UNIVERSITY OF CALIFORNIA, SAN DIEGO

Discourse on the Characterization of Waveguide Distributed Bragg Reflectors for Application to Nonlinear Optics

A dissertation submitted in partial satisfaction of the requirements for the degree Doctor of Philosophy

in

Electrical Engineering (Photonics)

by

Andrew Lewis Grieco

Committee in charge:

Professor Yeshaiahu Fainman, Chair
Professor Prabhakar Bandaru
Professor Andrew Kummel
Professor Zhaowei Liu
Professor Stojan Radic

2014

ProQuest LLC.
789 East Eisenhower Parkway
P.O. Box 1346
Ann Arbor, MI 48106 - 1346

The Dissertation of Andrew Lewis Grieco is approved, and it is acceptable in quality and form for publication on microfilm and electronically:

_____

_____

_____

_____

_____

Chair

University of California, San Diego

2014

TABLE OF CONTENTS

LIST OF FIGURES

ACKNOWLEDGEMENTS

This work was supported by the National Science Foundation (NSF), the NSF Engineering Research Center for Integrated Access Networks, the Defense Advanced Research Projects Agency, and the Cymer Corporation.

I would like to thank the Nano3 staff at UCSD and B. Mitchell at UCSB for support during sample fabrication, and C. Hennessey for logistical support.

Finally I would like to gratefully acknowledge those who provided invaluable guidance during my scientific education: Prof. Y. Fainman, Dr. B. Slutsky, Dr. D. S. Moore, Prof. K. Minschwaner, Prof. P. J. Boston, Mr. R. Grieco, and Mrs. V. Grieco. I am particularly indebted to my parents for fostering my sense of curiosity.

Chapter 2, in part, is a reprint of "Characterization of waveguide loss using distributed Bragg reflectors" by A. Grieco, B. Slutsky, and Y. Fainman as it appears in Applied Physics B, volume 114, Springer, 2014. The dissertation author was the primary author of this paper.

Chapter 3, in part, is a reprint of "Characterization of Distributed Bragg Reflectors" by A. Grieco, and Y. Fainman as it appears in the Journal of Quantum Electronics, volume 50, Institute of Electrical and Electronics Engineers (IEEE), 2014. The dissertation author was the primary author of this paper.

Chapter 4, in part, is a reprint of "Characterization of waveguide loss using distributed Bragg reflectors" by A. Grieco, B. Slutsky, and Y. Fainman as it appears in Applied Physics B, volume 114, Springer, 2014. The dissertation author was the primary author of this paper.

Chapter 5, in part, is a reprint of "Optical Bistability in a Silicon Waveguide Distributed Bragg Reflector Fabry-Pérot Resonator" by A. Grieco, B. Slutsky, D.T.H. Tan, S. Zamek, M. P. Nezhad, and Y. Fainman as it appears in the Journal of Lightwave Tecnology, volume 30, Institute of Electrical and Electronics Engineers (IEEE), 2012. The dissertation author was the primary author of this paper.

Chapter 6, in part, is a reprint of both "Optical Bistability in a Silicon Waveguide Distributed Bragg Reflector Fabry-Pérot Resonator" by A. Grieco, B. Slutsky, D.T.H. Tan, S. Zamek, M. P. Nezhad, and Y. Fainman as it appears in the Journal of Lightwave Tecnology, volume 30, Institute of Electrical and Electronics Engineers (IEEE), 2012, and "Characterization of waveguide loss using distributed Bragg reflectors" by A. Grieco, B. Slutsky, and Y. Fainman as it appears in Applied Physics B, volume 114, Springer, 2014, and "Characterization of Distributed Bragg Reflectors" by A. Grieco and Y. Fainman as it appears in the Journal of Quantum Electronics, volume 50, Institute of Electrical and Electronics Engineers (IEEE), 2014. The dissertation author was the primary author of these papers.

Chapter 7, in part, is a reprint of both "Optical Bistability in a Silicon Waveguide Distributed Bragg Reflector Fabry-Pérot Resonator" by A. Grieco, B. Slutsky, D.T.H. Tan, S. Zamek, M. P. Nezhad, and Y. Fainman as it appears in the Journal of Lightwave Tecnology, volume 30, Institute of Electrical and Electronics Engineers (IEEE), 2012, "Characterization of waveguide loss using distributed Bragg reflectors" by A. Grieco, B. Slutsky, and Y. Fainman as it appears in Applied Physics B, volume 114, Springer, 2014, and "Characterization of Distributed Bragg

Reflectors" by A. Grieco and Y. Fainman as it appears in the Journal of Quantum Electronics, volume 50, Institute of Electrical and Electronics Engineers (IEEE), 2014. The dissertation author was the primary author of these papers.

VITA

2007	Bachelor of Science in Earth Science (Geology) New Mexico Institute of Mining and Technology, Socorro, NM
2007	Bachelor of Science in Physics New Mexico Institute of Mining and Technology, Socorro, NM
2010	Master of Science in Electrical Engineering (Photonics) University of California, San Diego, San Diego, CA
2014	Doctor of Philosophy in Electrical Engineering (Photonics) University of California, San Diego, San Diego, CA

PUBLICATIONS

A. Grieco, and Y. Fainman, "Characterization of Distributed Bragg Reflectors," Journal of Quantum Electronics, vol. 50, pp. 453-457, Jun. 2014.

D.T.H. Tan, A. Grieco, T. Wang, G. F. R. Chen, and Y. Fainman, "Towards 100 Channel Dense Wavelength Division Multiplexing with 100GHz Spacing on Silicon," Optics Express, vol. 22, pp. 10408-10415, May 2014.

M. W. Puckett, J. S. T. Smalley, M. Abashin, A. Grieco, and Y. Fainman, "Tensor of the Second Order Nonlinear Susceptibility in Asymmetrically Strained Silicon Waveguides: Analysis and Experimental Validation," Optics Letters, vol. 39, pp. 1693-1696, Mar. 2014.

A. Grieco, B. Slutsky, and Y. Fainman, "Characterization of waveguide loss using distributed Bragg reflectors," Applied Physics B, vol. 114, pp. 467-474, Mar. 2014.

Y. Wang, A. Grieco, and T. Nguyen, "Allpass filter design with waveguide loss compensation," Optics Express, vol. 21, pp. 32040-32052, Dec. 2013.

Y. Fainman, M. P. Nezhad, D. T. H. Tan, K. Ikeda, O. Bondarenko, and A. Grieco, "Silicon nanophotonic devices for chip-scale optical communication applications [Invited]," Applied Optics, vol. 52, pp. 613-624, Jan. 2013.

A. Grieco, B. Slutsky, D.T.H. Tan, S. Zamek, M. P. Nezhad, and Y. Fainman, "Optical Bistability in a Silicon Waveguide Distributed Bragg Reflector Fabry-Pérot Resonator," Journal of Lightwave Technology, vol. 30, pp. 2352-2355, Jul. 2012.

S. D. McGrane, A. Grieco, K. J. Ramos, D. E. Hooks, and D. S. Moore, "Femtosecond micromachining of internal voids in high explosive crystals for studies of hot spot initiation," Journal of Applied Physics, vol. 105, pp. 073505-1-073505-7, Apr. 2009.

FIELDS OF STUDY

Major Field: Electrical Engineering

Studies in Photonics
Professor Yeshaiahu Fainman

ABSTRACT OF THE DISSERTATION

Discourse on the Characterization of Waveguide Distributed Bragg Reflectors for Application to Nonlinear Optics

by

Andrew Lewis Grieco

Doctor of Philosophy in Electrical Engineering (Photonics)

University of California, San Diego, 2014

Professor Yeshaiahu Fainman, Chair

Precise characterization of waveguide parameters is necessary for the successful design of nonlinear photonic devices. This dissertation contains a description of methods for the experimental characterization of distributed Bragg reflectors for use in nonlinear optics and other applications. The general coupled-mode

theory of Bragg reflection arising from a periodic dielectric perturbation is developed from Maxwell's equations. This theory is then applied to develop a method of characterizing the fundamental parameters that describe Bragg reflection by comparing the spectral response of Bragg reflector resonators. This method is also extended to characterize linear loss in waveguides. A model of nonlinear effects in Bragg reflector resonators manifesting in bistability is also developed, as this phenomenon can be detrimental to the characterization method. Specific recommendations are made regarding waveguide fabrication and experimental design to reduce sources of experimental error.

1. Introduction and Motivation

This dissertation contains a description of methods for the experimental characterization of distributed Bragg reflectors and associated waveguide elements. The impetus for the development of these methods arose from the desire to perform nonlinear wave mixing within a resonant cavity comprised of Bragg reflectors. In principle the field accumulation within the resonator should increase the efficiency of the process, provided certain phase matching conditions are met. All attempts at fabricating such a device ended in failure, despite a sound theoretical understanding of the underlying physics. The cause of the failures was imprecision in the estimate of parameters that governed the resonator behavior, because the nonlinear operation of the resonator is extremely sensitive to these parameters. This situation essentially rendered design of the correct device impossible without resorting to attrition or serendipity.

In this situation the only recourse was to develop a method of characterizing the device parameters, taking care to eliminate as many sources of uncertainty as possible. The effort was successful, producing a method that is independent of coupling efficiency, does not require bending of the waveguide, and occupies a minimal footprint. In the pursuit of this object it was necessary to develop the coupled-mode theory of Bragg reflection in the most general case of mode interaction.

The remainder of the dissertation is organized as follows. Chapter 2 contains a theoretical description of Bragg reflection developed from Maxwell's equations. Chapter 3 describes a method of experimentally characterizing the parameters that govern Bragg reflection between arbitrary modes, namely the linear loss coefficients of the perturbed waveguide modes, and the coupling coefficients. Chapter 4 describes a method of experimentally characterizing the linear loss coefficients of unperturbed waveguide modes. Chapter 5 contains a description of the phenomena of bistability that can arise in nonlinear resonators, and which has the potential to introduce error into the characterization measurements. Chapters 6 and 7 respectively contain a description of the waveguide fabrication procedure, and experimental design process, and contain recommendations to reduce sources of experimental error.

2. Theory of Distributed Bragg Reflectors

2.1. Maxwell's Equations

The mathematical theory of distributed Bragg reflectors begins with Maxwell's equations that describe the relationship between the electromagnetic fields [1]:

$$\nabla \cdot \mathbf{D} = \rho \,, \tag{2.1}$$

$$\nabla \times \mathbf{H} - \frac{\partial \mathbf{D}}{\partial t} = \mathbf{J} \,, \tag{2.2}$$

$$\nabla \times \mathbf{E} + \frac{\partial \mathbf{B}}{\partial t} = 0 \,, \tag{2.3}$$

$$\nabla \cdot \mathbf{B} = 0 \,, \tag{2.4}$$

where **E** and **H** are respectively the electric and the magnetic field vectors, **D** and **B** are respectively the electric displacement and magnetic induction field vectors, ρ is the electric charge density, and **J** is the electric current density. Within a material, the fields **E** and **H** are related to the fields **D** and **B** through the constitutive equations:

$$\mathbf{D} = \varepsilon \mathbf{E} = \varepsilon_0 \mathbf{E} + \mathbf{P} \,, \tag{2.5}$$

$$\mathbf{B} = \mu \mathbf{H} = \mu_0 \mathbf{H} + \mathbf{M} ,$$

(2.6)

where the material permittivity ε and permeability μ are tensors (the subscript 0 indicates their values in vacuum), and vector fields **P** and **M** are respectively the material electric and magnetic polarization. It should be noted that Eqs. (2.5) and (2.6) are not strictly the most general form that these relations may assume. In the most general sense the **D** and **B** fields may be related to the **E** and **H** fields in a way that involves additional complexities such as nonlinearity and hysteresis.

2.2. The Electromagnetic Wave Equation

Now consider the limit of homogenous materials in which the nonlinearities and anisotropy are negligible such that ε and μ may be taken as scalars (or in the case of anisotropy such that the fields are aligned with a principle axis), and in which the charge density ρ and the current density **J** are also negligible. Under these circumstances, the electromagnetic wave equation may be derived by first applying the curl operator to Eqs. (2.2) and (2.3) and then invoking Eqs. (2.5) and (2.6) [2]:

$$\nabla \times \left(\nabla \times \mathbf{E} \right) + \mu \frac{\partial}{\partial t} \left(\nabla \times \mathbf{H} \right) = 0 ,$$

(2.7)

$$\nabla \times \left(\nabla \times \mathbf{H} \right) - \varepsilon \frac{\partial}{\partial t} \left(\nabla \times \mathbf{E} \right) = 0 .$$

(2.8)

The mixed fields in Eqs. (2.7) and (2.8) may be separated through substitution of the time derivatives of Eqs. (2.2) and (2.3), and again invoking Eqs. (2.5) and (2.6):

$$\nabla \times \left(\nabla \times \mathbf{E} \right) + \mu\varepsilon \frac{\partial^2 \mathbf{E}}{\partial t^2} = 0 \ ,$$

(2.9)

$$\nabla \times \left(\nabla \times \mathbf{H} \right) + \mu\varepsilon \frac{\partial^2 \mathbf{H}}{\partial t^2} = 0 \, .$$

(2.10)

From Eqs. (2.9) and (2.10) the wave equation is a consequence of the vector identity:

$$\nabla \times \left(\nabla \times \mathbf{A} \right) = \nabla \left(\nabla \cdot \mathbf{A} \right) - \nabla^2 \mathbf{A} \, ,$$

(2.11)

and the observation that the fields are divergence free from Eqs. (2.1) and (2.4):

$$\nabla^2 \mathbf{E} = \mu\varepsilon \frac{\partial^2 \mathbf{E}}{\partial t^2} = \frac{n^2}{c^2} \frac{\partial^2 \mathbf{E}}{\partial t^2} \ ,$$

(2.12)

$$\nabla^2 \mathbf{H} = \mu\varepsilon \frac{\partial^2 \mathbf{H}}{\partial t^2} = \frac{n^2}{c^2} \frac{\partial^2 \mathbf{H}}{\partial t^2} \, ,$$

(2.13)

$$c = 1 \Big/ \sqrt{\varepsilon_0 \mu_0} \ ,$$

(2.14)

$$n = \sqrt{\varepsilon\mu} \Big/ \sqrt{\varepsilon_0 \mu_0} \ . \tag{2.15}$$

where c is the speed of light propagating in vacuum, and n is the material refractive index. The refractive index thus represents the factor by which the velocity of light in a material differs from the velocity of light in vacuum.

In the absence of additional constraints, the solutions of Eqs. (2.12) and (2.13) for the Cartesian vector components of **E** and **H** are plane waves. In the presence of additional boundary conditions (such as the interface of multiple materials) the solution becomes more complicated [3]. For a general combination of materials that is homogeneous in the z-direction the permittivity and permeability will assume the form:

$$\varepsilon(x, y, z, t) = \varepsilon(x, y), \tag{2.16}$$

$$\mu(x, y, z, t) = \mu(x, y), \tag{2.17}$$

where x, y and z are the Cartesian coordinates, and t is the time coordinate. When Eqs. (2.12) and (2.13) are subjected to the conditions imposed by Eqs. (2.16) and (2.17), the solution of the wave equations will be composed of normal modes of the form:

$$\mathbf{E}(x, y, z, t) = \mathrm{Re}\{\mathbf{E}_m(x, y)\exp[i(\omega t - \beta_m z)]\}, \tag{2.18}$$

$$\mathbf{H}(x,y,z,t) = \mathrm{Re}\{\mathbf{H}_m(x,y)\exp[i(\omega t - \beta_m z)]\},$$

(2.19)

where ω is the angular frequency of the field, β is the propagation constant, and m is a subscript used to distinguish multiple modes. In the most general case the mode subscript may be discrete (as in the case of guided modes) or continuous (as in the case of radiative modes). Within scientific literature the complex field formalism is commonly employed, such that taking the real part of the fields is implied rather than written explicitly. Although analytical solutions to the wave equation are known for a number of material geometries, in the most cases the solution must be computed numerically [4]. Finally, it is pertinent to observe the method of solution assuming z invariance in the permittivity and permeability may be extended to the cases of geometries with z variance using the technique of conformal mapping [5], [6]. This is particularly useful for the analysis of curved waveguides.

2.3. Electromagnetic Energy

2.3.1. Energy and Power Density

The power density of the electric fields can be obtained by projecting the electric field vector **E** onto Eq. (2.2) [2]:

$$\mathbf{E}\cdot(\nabla\times\mathbf{H}) - \mathbf{E}\cdot\frac{\partial\mathbf{D}}{\partial t} = \mathbf{E}\cdot\mathbf{J}\,.$$

(2.20)

From application of the following vector identity:

$$\nabla \cdot (\mathbf{A} \times \mathbf{B}) = \mathbf{B} \cdot (\nabla \times \mathbf{A}) - \mathbf{A} \cdot (\nabla \times \mathbf{B})$$

(2.21)

Eq. (2.20) may be rewritten as:

$$\nabla \cdot (\mathbf{H} \times \mathbf{E}) + \mathbf{H} \cdot (\nabla \times \mathbf{E}) - \mathbf{E} \cdot \frac{\partial \mathbf{D}}{\partial t} = \mathbf{E} \cdot \mathbf{J} \,.$$

(2.22)

By substitution of Eq. (2.3) the expression becomes:

$$\nabla \cdot \mathbf{S} + \frac{\partial U}{\partial t} = -\mathbf{E} \cdot \mathbf{J} \,,$$

(2.23)

$$\mathbf{S} = \mathbf{E} \times \mathbf{H} \,,$$

(2.24)

$$U = \frac{1}{2}(\mathbf{E} \cdot \mathbf{D} + \mathbf{B} \cdot \mathbf{H}) \,,$$

(2.25)

where Poynting's vector **S** is the power density of the fields, and U is the energy density of the fields.

2.3.2. Energy Velocity

For monochromatic fields that assume the form of Eqs. (2.18) and (2.19) the surfaces of constant phase of the modes are defined by the condition [2]:

$$\omega t - \beta_m z = \text{constant}.$$

(2.26)

From the time derivative of Eq. (2.26) it is obvious that the fields (and from Eq. (2.25) the energy associated with the fields) propagate along the z-direction at the phase velocity v_p:

$$v_p = \frac{\omega}{\beta_m} = \frac{\omega}{n_{eff}\beta_0},$$

(2.27)

$$n_{eff} = \frac{\beta_m}{\beta_0} = \frac{c}{v_p},$$

(2.28)

where the ratio of the mode propagation constant β_m to the vacuum propagation constant β_0 is referred to as the effective refractive index of the mode n_{eff}, and c is the vacuum velocity of light.

For polychromatic fields, the question of energy propagation is more complicated [7]. To demonstrate this, represent the mode of a polychromatic wave as the Fourier transform:

$$\mathbf{A}(x,y,z,t) = \int_{-\infty}^{\infty} \mathbf{A}(x,y,\omega)\exp\{i[\omega t - \beta(\omega)z]\}d\omega,$$

(2.29)

where **A** is the amplitude of either the electric or magnetic field. Note that the form of Eq. (2.29) is in accordance with the exponentials of Eqs. (2.18) and (2.19) provided that the mode index can be expressed as a continuous function of frequency. As an additional restriction, consider only spectrally narrow fields such that $\mathbf{A}(x,y,\omega)$ is negligible outside of a narrow peak around $\omega = \omega_0$. To elucidate the time evolution of the such a field, expand $\beta(\omega)$ in a Taylor series about its central value β_0:

$$\beta(\omega) = \beta(\omega_0) + \left(\frac{d\beta}{d\omega}\right)_0 (\omega - \omega_0) + \ldots ,$$

(2.30)

where the higher order terms are rendered negligible by the frequency restriction. Substitution of Eq. (2.30) into Eq. (2.29) produces an expression of the form:

$$\begin{aligned}\mathbf{A}(x,y,z,t) &\approx \int_{-\infty}^{\infty} \mathbf{A}(x,y,\omega)\exp\left\{i\left[\omega t - \beta(\omega_0)z - \left(\frac{d\beta}{d\omega}\right)_0 (\omega - \omega_0)z\right]\right\}d\omega \\ &= \exp\left\{i\left[-\beta(\omega_0)z + \left(\frac{d\beta}{d\omega}\right)_0 \omega_0 z\right]\right\}\int_{-\infty}^{\infty} \mathbf{A}(x,y,\omega)\exp\left\{i\left[\omega t - \left(\frac{d\beta}{d\omega}\right)_0 \omega z\right]\right\}d\omega\end{aligned},$$

(2.31)

which has a magnitude of:

$$|\mathbf{A}(x,y,z,t)| \approx \left|\int_{-\infty}^{\infty} \mathbf{A}(x,y,\omega)\exp\left\{i\left[\omega t - \left(\frac{d\beta}{d\omega}\right)_0 \omega z\right]\right\}d\omega\right| .$$

(2.32)

The field thus behaves as a wave packet with the surfaces of constant phase of the envelope defined by the condition:

$$\omega t - \left(\frac{d\beta}{d\omega}\right)_0 \omega z = \text{constant} .$$

(2.33)

From the time derivative of Eq. (2.33) it is clear that the wave packet (and by Eq. (2.25) the energy associated with the wave packet) propagate along the *z*-direction at the so called group velocity v_g:

$$v_g = \frac{d\omega}{d\beta} .$$

(2.34)

such that the derivative is taken about the central frequency. It is convention to define a group index n_g that is analogous to the refractive index, except that it relates to the group velocity instead of the phase velocity:

$$n_g = \frac{c}{v_g} .$$

(2.35)

2.3.3. Time Averaged Energy and Power

From an experimental standpoint, it is often not feasible to measure the instantaneous power of a high frequency electromagnetic field. In this situation it becomes necessary instead to measure the time averaged power and energy [4]. From Eq. (2.24), the expression of power density **S** for a monochromatic time harmonic field is:

$$
\begin{aligned}
\mathbf{S} &= \mathrm{Re}\left[\mathbf{E}(x,y,z)\exp(i\omega t)\right]\times \mathrm{Re}\left[\mathbf{H}(x,y,z)\exp(i\omega t)\right] \\
&= \frac{1}{2}\left[\mathbf{E}\exp(i\omega t)+\mathbf{E}^{*}\exp(-i\omega t)\right]\times\frac{1}{2}\left[\mathbf{H}\exp(i\omega t)+\mathbf{H}^{*}\exp(-i\omega t)\right] \\
&= \frac{1}{4}\left[\mathbf{E}\times\mathbf{H}^{*}+\mathbf{E}^{*}\times\mathbf{H}\right]+\frac{1}{4}\left[\mathbf{E}\times\mathbf{H}\exp(2i\omega t)+\mathbf{E}^{*}\times\mathbf{H}^{*}\exp(-2i\omega t)\right] \\
&= \frac{1}{2}\left\{\frac{1}{2}\left[\mathbf{E}\times\mathbf{H}^{*}+\left(\mathbf{E}\times\mathbf{H}^{*}\right)^{*}\right]+\frac{1}{2}\left[\mathbf{E}\times\mathbf{H}\exp(2i\omega t)+\left(\mathbf{E}\times\mathbf{H}\right)^{*}\exp(2i\omega t)^{*}\right]\right\} \\
&= \frac{1}{2}\left\{\mathrm{Re}\left[\mathbf{E}\times\mathbf{H}^{*}\right]+\frac{1}{2}\mathrm{Re}\left[\mathbf{E}\times\mathbf{H}\exp(2i\omega t)\right]\right\}
\end{aligned}
\qquad (2.36)
$$

where the and the * operator indicates complex conjugation and the explicit dependence on spatial coordinates is suppressed in the latter equations. Since the fields are periodic, the time averaging may be performed over a single period *T*. Thus the time averaged power density $\mathbf{S}_{avg}$ of Eq. (2.36) is:

$$
\mathbf{S}_{avg} = \frac{1}{T}\int_{0}^{T}\frac{1}{2}\left\{\mathrm{Re}\left[\mathbf{E}\times\mathbf{H}^{*}\right]+\mathrm{Re}\left[\mathbf{E}\times\mathbf{H}\exp(2i\omega t)\right]\right\}dt = \frac{1}{2}\mathrm{Re}\left[\mathbf{E}(x,y,z)\times\mathbf{H}(x,y,z)^{*}\right].
\qquad (2.37)
$$

The energy density may be treated similarly. Substitution of a monochromatic time harmonic field into Eq. (2.25) produces:

$$
\begin{aligned}
U &= \frac{1}{2}\left\{\mathrm{Re}\left[\mathbf{E}\exp(i\omega t)\right]\cdot\mathrm{Re}\left[\mathbf{D}\exp(i\omega t)\right]+\mathrm{Re}\left[\mathbf{B}\exp(i\omega t)\right]\cdot\mathrm{Re}\left[\mathbf{H}\exp(i\omega t)\right]\right\} \\
&= \frac{1}{2}\left\{\begin{array}{l}\frac{1}{2}\left[\mathbf{E}\exp(i\omega t)+\mathbf{E}^{*}\exp(-i\omega t)\right]\cdot\frac{1}{2}\left[\mathbf{D}\exp(i\omega t)+\mathbf{D}^{*}\exp(-i\omega t)\right] \\ +\frac{1}{2}\left[\mathbf{B}\exp(i\omega t)+\mathbf{B}^{*}\exp(-i\omega t)\right]\cdot\frac{1}{2}\left[\mathbf{H}\exp(i\omega t)+\mathbf{H}^{*}\exp(-i\omega t)\right]\end{array}\right\} \\
&= \frac{1}{4}\left\{\begin{array}{l}\frac{1}{2}\left[\mathbf{E}\cdot\mathbf{D}^{*}+\mathbf{E}^{*}\cdot\mathbf{D}\right]+\frac{1}{2}\left[\mathbf{E}\cdot\mathbf{D}\exp(2i\omega t)+\mathbf{E}^{*}\cdot\mathbf{D}^{*}\exp(-2i\omega t)\right] \\ \frac{1}{2}\left[\mathbf{B}\cdot\mathbf{H}^{*}+\mathbf{B}^{*}\cdot\mathbf{H}\right]+\frac{1}{2}\left[\mathbf{B}\cdot\mathbf{H}\exp(2i\omega t)+\mathbf{B}^{*}\cdot\mathbf{H}^{*}\exp(-2i\omega t)\right]\end{array}\right\} \\
&= \frac{1}{4}\left\{\mathrm{Re}\left[\mathbf{E}\cdot\mathbf{D}^{*}\right]+\mathrm{Re}\left[\mathbf{B}\cdot\mathbf{H}^{*}\right]+\mathrm{Re}\left[\mathbf{E}\cdot\mathbf{D}\exp(2i\omega t)\right]+\mathrm{Re}\left[\mathbf{B}\cdot\mathbf{H}\exp(2i\omega t)\right]\right\}
\end{aligned}
,
$$

(2.38)

where the explicit spatial dependence of the fields has again been suppressed. Following the same reasoning as before, the time averaged energy density U_{avg} of Eq. (2.38) is:

$$
\begin{aligned}
U_{avg} &= \frac{1}{T}\int_{0}^{T}\frac{1}{4}\left\{\mathrm{Re}\left[\mathbf{E}\cdot\mathbf{D}^{*}\right]+\mathrm{Re}\left[\mathbf{B}\cdot\mathbf{H}^{*}\right]+\mathrm{Re}\left[\mathbf{E}\cdot\mathbf{D}\exp(2i\omega t)\right]+\mathrm{Re}\left[\mathbf{B}\cdot\mathbf{H}\exp(2i\omega t)\right]\right\}dt \\
&= \frac{1}{4}\mathrm{Re}\left[\mathbf{E}(x,y,z)\cdot\mathbf{D}^{*}(x,y,z)+\mathbf{B}(x,y,z)\cdot\mathbf{H}^{*}(x,y,z)\right]
\end{aligned}
.
$$

(2.39)

It is clear by inspection that Eqs. (2.37) and (2.39) are applicable to electromagnetic modes assuming the form of Eqs. (2.18) and (2.19).

2.4. Orthonormalization of Electromagnetic Modes

It is easy to demonstrate that modes of the form of Eqs. (2.18) and (2.19) display an orthogonality relationship by considering the spatial characteristics of the

associated electromagnetic power flow. This is similar to the conventional method [3], although it does not invoke the Lorentz reciprocity theorem. Specifically, since the permittivity and permeability are invariant along the direction of field propagation, the time averaged power of the fields must be constant along the propagation direction (provided that field loss is negligible). Following Eqs. (2.18) and (2.19), when multiple modes are excited the total electric and magnetic fields are:

$$\mathbf{E}(x,y,z,t) = \mathrm{Re}\left\{\sum_l \mathbf{E}_l(x,y)\exp[i(\omega t - \beta_l z)]\right\},$$

(2.40)

$$\mathbf{H}(x,y,z,t) = \mathrm{Re}\left\{\sum_m \mathbf{H}_m(x,y)\exp[i(\omega t - \beta_m z)]\right\}.$$

(2.41)

From substitution of Eqs. (2.40) and (2.41) into Eq. (2.37), the total time averaged power $\mathbf{P}_{Tot}$ is therefore:

$$\begin{aligned}\mathbf{P}_{Tot} &= \int_{-\infty}^{\infty}\int_{-\infty}^{\infty}\frac{1}{2}\mathrm{Re}\left\{\left[\sum_l \mathbf{E}_l(x,y)\exp(-i\beta_l z)\right]\times\left[\sum_m \mathbf{H}_m(x,y)^*\exp(i\beta_m z)\right]\cdot\mathbf{n}_z\right\}dxdy \\ &= \frac{1}{2}\mathrm{Re}\left\{\sum_l\sum_m \exp[i(\beta_m-\beta_l)z]\int_{-\infty}^{\infty}\int_{-\infty}^{\infty}\mathbf{E}_l(x,y)\times\mathbf{H}_m(x,y)^*\cdot\mathbf{n}_z dxdy\right\}\end{aligned},$$

(2.42)

where $\mathbf{n}_z$ is a unit vector along the z-direction. The condition of constant power flow applied to Eq. (2.42) thus becomes:

$$0 = \frac{\partial \mathbf{P}_{Tot}}{\partial z} = \frac{1}{2}\mathrm{Re}\left\{ \left(\beta_m - \beta_l\right) \sum_l \sum_m \exp\left[i\left(\beta_m - \beta_l\right)z\right] \int_{-\infty}^{\infty}\int_{-\infty}^{\infty} \mathbf{E}_l(x,y) \times \mathbf{H}_m(x,y)^* \cdot \mathbf{n}_z dxdy \right\}. \tag{2.43}$$

By inspection of Eq. (2.43), it is evident that the following orthogonality condition must be obeyed by the fields:

$$\frac{1}{2}\mathrm{Re}\left[\int_{-\infty}^{\infty}\int_{-\infty}^{\infty} \mathbf{E}_l(x,y) \times \mathbf{H}_m(x,y)^* \cdot \mathbf{n}_z dxdy \right] = 0, \tag{2.44}$$

for $l \neq m$. The form of Eq. (2.44) suggests the following orthonormalization condition for the fields:

$$\left| \frac{1}{2}\mathrm{Re}\left[\int_{-\infty}^{\infty}\int_{-\infty}^{\infty} \mathbf{E}_l(x,y) \times \mathbf{H}_m(x,y)^* \cdot \mathbf{n}_z dxdy \right] \right| = \delta_{lm}, \tag{2.45}$$

where δ_{lm} is the Kronecker delta (taken as having units of power), and the modes are normalized to unity (the absolute value included because the sign of the power flow will depend on the propagation direction).

From the relationship between electromagnetic power and energy flow, it is possible to infer additional constraints between the fields of an electromagnetic wave. Specifically, it is possible to demonstrate the equality of the energy separately associated with the electric and magnetic fields. The equality follows from relating the

energy velocity from Eqs. (2.27) or (2.34), with the power density of Eq. (2.24), and the energy density of Eq. (2.25):

$$\mathbf{E}\times\mathbf{H}=\mathbf{v}\frac{1}{2}\left(\mathbf{E}\cdot\mathbf{D}+\mathbf{B}\cdot\mathbf{H}\right),$$

(2.46)

where **v** is the relevant energy velocity. Substitution of the constitutive relations from Eqs. (2.5) and (2.6) into Eq. (2.46) simplifies to:

$$\mathbf{E}\times\mathbf{H}=\mathbf{v}\frac{1}{2}\left(\varepsilon\,\mathbf{E}\cdot\mathbf{E}+\mu\,\mathbf{E}\cdot\mathbf{E}\right).$$

(2.47)

Dividing Eq. (2.47) by both field magnitudes results in the relationship:

$$\mathbf{n}_E\times\mathbf{n}_H=\mathbf{v}\frac{1}{2}\left(\varepsilon\frac{|\mathbf{E}|}{|\mathbf{H}|}+\mu\frac{|\mathbf{H}|}{|\mathbf{E}|}\right).$$

(2.48)

where $\mathbf{n}_E$ and $\mathbf{n}_H$ are unit vectors oriented respectively in the direction of the electric and magnetic fields. Noting that the velocity is constant, applying separately the divergence and curl operators to Eq. (2.48) results in the following conditions:

$$\nabla\cdot\left(\mathbf{n}_E\times\mathbf{n}_H\right)=0=\mathbf{v}\cdot\nabla\left[\frac{1}{2}\left(\varepsilon\frac{|\mathbf{E}|}{|\mathbf{H}|}+\mu\frac{|\mathbf{H}|}{|\mathbf{E}|}\right)\right],$$

(2.49)

$$\nabla \times \left(\mathbf{n}_E \times \mathbf{n}_H \right) = 0 = \mathbf{v} \times \nabla \left[\frac{1}{2} \left(\varepsilon \frac{|\mathbf{E}|}{|\mathbf{H}|} + \mu \frac{|\mathbf{H}|}{|\mathbf{E}|} \right) \right].$$

(2.50)

The simultaneous conditions of Eqs. (2.49) and (2.50) imply that the gradient term must vanish, since it possesses no components either parallel or perpendicular to the velocity. This term may be expanded as:

$$0 = \nabla \left[\frac{1}{2} \left(\varepsilon \frac{|\mathbf{E}|}{|\mathbf{H}|} + \mu \frac{|\mathbf{H}|}{|\mathbf{E}|} \right) \right] = \frac{1}{2} \left(\varepsilon - \mu \frac{|\mathbf{H}|^2}{|\mathbf{E}|^2} \right) \nabla \left(\frac{|\mathbf{E}|}{|\mathbf{H}|} \right).$$

(2.51)

The gradient of the field ratio in the last term of Eq. (2.51) does not vanish in general. This means the equality is only satisfied when its leading term vanishes:

$$0 = \frac{1}{2} \left(\varepsilon - \mu \frac{|\mathbf{H}|^2}{|\mathbf{E}|^2} \right).$$

(2.52)

The equality of Eq. (2.52) is only satisfied when the electric and magnetic energy density terms are equal:

$$\frac{1}{2} \varepsilon |\mathbf{E}|^2 = \frac{1}{2} \mu |\mathbf{H}|^2.$$

(2.53)

Therefore the electric and magnetic energy density of an electromagnetic wave propagating at constant velocity must be equal. Combining Eqs. (2.45), (2.37), and

(2.53), the orthonormalization condition may be conveniently rewritten in terms of a single field:

$$\frac{v}{4}\int_{-\infty}^{\infty}\int_{-\infty}^{\infty}\varepsilon\,\mathbf{E}_l\cdot\mathbf{E}_m^{*}\,dxdy=\frac{v}{4}\int_{-\infty}^{\infty}\int_{-\infty}^{\infty}\mu\,\mathbf{H}_l\cdot\mathbf{H}_m^{*}\,dxdy=\delta_{lm}\,,$$

(2.54)

where v is the magnitude of the energy velocity.

Strictly, the equality of electric and magnetic energy arising from Eq. (2.51) is only valid when the gradient of the permittivity and permeability is negligible. This will be applicable to waveguides comprised of homogenous materials, but not to those in which the refractive index is graded. A more general proof exists based on the Lorentz reciprocity theorem that is applicable to graded index materials [8]. Interestingly, the orthonormalization condition of Eq. (2.54) can be arrived at for a given field purely from the existence of modal solutions to Maxwell's equations. This is because the field amplitudes of a mode may only be scaled together (which represents the freedom to scale the total energy in the mode). Otherwise the relationship between the fields is fixed. Thus for a given modal solution the relative amplitudes of the electric and magnetic fields may be written as:

$$\mathbf{E}_l=c_l\mathbf{H}_l\,,$$

(2.55)

where c_l is some constant, and the subscript l indicates modal association. Substitution of Eq. (2.55) into Eq. (2.47) results in the relationships:

$$\mathbf{E}_l \times \mathbf{H}_l = \mathbf{v}\frac{1}{2}\left(\varepsilon|c_l|^2 + \mu\right)\mathbf{H}_l \cdot \mathbf{H}_l ,$$

(2.56)

$$\mathbf{E}_l \times \mathbf{H}_l = \mathbf{v}\frac{1}{2}\left(\varepsilon + \frac{\mu}{|c_l|^2}\right)\mathbf{E}_l \cdot \mathbf{E}_l .$$

(2.57)

Since the energy may be normalized arbitrarily, it is possible to choose a normalization such that either the electric field energy or the magnetic field energy is normalized to unity (although in general not both at the same time). For such a situation the orthonormalization condition of Eq. (2.54) for the selected field follows directly from Eq. (2.57), and it holds for the remaining field up to a multiplicative constant. This is a more general derivation in the sense that it holds even for cases in which the electric and magnetic energy are not equal.

2.5. Coupled-Mode Theory of Bragg Reflection

2.5.1. The Lorentz Reciprocity Theorem

The most general approach to electromagnetic coupled-mode theory relies on a result known as the Lorentz reciprocity theorem [8], [9]. To arrive at this theorem, consider arbitrary solutions to Maxwell's Equations for a pair of distinct waveguides denoted by **E**, **H** and **E'**, **H'** respectively in a nonmagnetic dielectric. For time-harmonic solutions at a fixed frequency Eqs. (2.1)-(2.4), Maxwell's equations, reduce to:

$$\begin{aligned} \nabla \times \mathbf{E} &= -i\omega\mu\mathbf{H} \\ \nabla \times \mathbf{H} &= i\omega\varepsilon\mathbf{E} \end{aligned}, \tag{2.58}$$

and

$$\begin{aligned} \nabla \times \mathbf{E}' &= -i\omega\mu\mathbf{H}' \\ \nabla \times \mathbf{H}' &= i\omega\varepsilon'\mathbf{E}' \end{aligned}. \tag{2.59}$$

By application of the vector identity from Eq. (2.21) the solutions from Eqs. (2.58) and (2.59) may be written as:

$$\begin{aligned} \nabla \cdot \left(\mathbf{E}^* \times \mathbf{H}'\right) &= \mathbf{H}' \cdot \nabla \times \mathbf{E}^* - \mathbf{E}^* \cdot \nabla \times \mathbf{H}' = \mathbf{H}' \cdot i\omega\mu\mathbf{H}^* + \mathbf{E}^* \cdot i\omega\varepsilon'\mathbf{E}' \\ \nabla \cdot \left(\mathbf{E}' \times \mathbf{H}^*\right) &= \mathbf{H}^* \cdot \nabla \times \mathbf{E}' - \mathbf{E}' \cdot \nabla \times \mathbf{H}^* = \mathbf{H}^* \cdot -i\omega\mu\mathbf{H}' + \mathbf{E}' \cdot -i\omega\varepsilon\mathbf{E}^* \end{aligned}. \tag{2.60}$$

Addition of the pair of terms in Eq. (2.60) results in the relationship known as the Lorentz reciprocity theorem:

$$\nabla \cdot \left(\mathbf{E}^* \times \mathbf{H}'\right) + \nabla \cdot \left(\mathbf{E}' \times \mathbf{H}^*\right) = -i\omega\left(\varepsilon' - \varepsilon\right)\mathbf{E}^* \cdot \mathbf{E}'. \tag{2.61}$$

It is pertinent to note that, although only the case of differing permittivity between the two solutions was considered here, the exact same method may be applied in the case of differing permeability, or in the case where they both differ simultaneously.

To apply the Lorentz reciprocity theorem in the context of waveguides, integrate each side of Eq. (2.61) over an arbitrary volume, and to the left side apply Gauss' theorem:

$$\iiint_V \nabla \cdot \mathbf{A} dV = \iint_{\partial S} \mathbf{A} \cdot d\mathbf{S},$$

(2.62)

such that:

$$\iint_{\partial S} \left(\mathbf{E}^* \times \mathbf{H}' + \mathbf{E}' \times \mathbf{H}^* \right) \cdot d\mathbf{S} = -i\omega \iiint_V (\varepsilon' - \varepsilon) \mathbf{E}^* \cdot \mathbf{E}' \, dV .$$

(2.63)

Consider Eq. (2.63) for a guided mode in the limit that the transverse integral is taken infinitely far from the waveguide, and that the integral in the direction of propagation is infinitesimally small. Taking z as the propagation direction, since the guided modes vanish at infinity the integral reduces to:

$$\lim_{\Delta z \to 0} \left\{ \iint_S \left[\left(\mathbf{E}^* \times \mathbf{H}' + \mathbf{E}' \times \mathbf{H}^* \right)_{z+\Delta z} - \left(\mathbf{E}^* \times \mathbf{H}' + \mathbf{E}' \times \mathbf{H}^* \right)_z \right] \cdot \mathbf{n}_z = -i\omega \Delta z \iint_S (\varepsilon' - \varepsilon) \mathbf{E}^* \cdot \mathbf{E}' \, dS \right\},$$

(2.64)

such that:

$$\iint_S \frac{\partial}{\partial z} \left(\mathbf{E}^* \times \mathbf{H}' + \mathbf{E}' \times \mathbf{H}^* \right) \cdot \mathbf{n}_z \, dS = -i\omega \iint_S (\varepsilon' - \varepsilon) \mathbf{E}^* \cdot \mathbf{E}' \, dS .$$

(2.65)

It is from consideration of Eq. (2.63) in the appropriate limits that the coupled-mode equations will arise.

2.5.2. Mode Coupling

The modes of Eq. (2.18) are believed to form a complete set, such that an arbitrary field may be expressed as [3]:

$$\mathbf{E}(x,y,z,t) = \mathrm{Re}\left\{\sum_l A_l \mathbf{E}_l(x,y)\exp\left[i(\omega t - \beta_l z)\right]\right\}$$
$$\mathbf{H}(x,y,z,t) = \mathrm{Re}\left\{\sum_l A_l \mathbf{H}_l(x,y)\exp\left[i(\omega t - \beta_l z)\right]\right\}. \tag{2.66}$$

where A_l is a constant term reflecting the contribution of each mode, and the mode coefficient l is summed over all modes. Consider a perturbation of the permittivity $\Delta\varepsilon$ such that:

$$\varepsilon(x,y,z,t) = \varepsilon(x,y) + \Delta\varepsilon(x,y,z). \tag{2.67}$$

Formally, an arbitrary field within the perturbed region may be expressed in terms of the normal modes of the unperturbed region. However, since the normal modes of the unperturbed region are not eigenmodes of the perturbed region, the A_l coefficients must generally become z dependent:

$$\mathbf{E}(x,y,z,t) = \mathrm{Re}\left\{\sum_l A_l(z)\mathbf{E}_l(x,y)\exp\left[i(\omega t - \beta_l z)\right]\right\}$$
$$\mathbf{H}(x,y,z,t) = \mathrm{Re}\left\{\sum_l A_l(z)\mathbf{H}_l(x,y)\exp\left[i(\omega t - \beta_l z)\right]\right\}.$$

(2.68)

By definition, the fields of both Eq. (2.66) and Eq. (2.68) obey Maxwell's equations.

The coupled mode equations may be derived by respectively associating the perturbed and unperturbed modal decompositions of Eqs. (2.68) and (2.66) with the primed and unprimed fields of the Lorentz reciprocity theorem as expressed in Eq. (2.65) [8], [9]. This substitution produces the relationship:

$$\sum_m \left[i(\beta_l - \beta_m)A_m(z) + \frac{dA_m(z)}{dz} \right] \exp\left[i(\beta_l - \beta_m)z\right] \iint \left(\mathbf{E}_l^* \times \mathbf{H}_m + \mathbf{E}_m \times \mathbf{H}_l^*\right) \cdot \mathbf{n}_z \, dxdy$$
$$= -i\omega \sum_m A_m(z)\exp\left[i(\beta_l - \beta_m)z\right] \iint \Delta\varepsilon \, \mathbf{E}_m \cdot \mathbf{E}_l^* \, dxdy.$$

(2.69)

In deriving Eq. (2.69) one minor optional simplification was made. Technically the *z*-component of the perturbed electric field differs from the transverse components by a constant factor. This may be seen by substituting the perturbed fields into Eqs. (2.1)-(2.4), Maxwell's equations, and expressing them in terms of the unperturbed modes:

$$\mathbf{E}(x,y,z)' = \frac{\nabla_\perp \times \mathbf{H}(x,y,z)'}{-i\omega(\varepsilon + \Delta\varepsilon)} = \frac{\sum_m A_m(z)\exp(-i\beta_m z)\nabla_\perp \times \mathbf{H}(x,y)_m}{-i\omega(\varepsilon + \Delta\varepsilon)}$$
$$= \frac{\varepsilon}{\varepsilon + \Delta\varepsilon} \sum_m A_m(z)\exp(-i\beta_m z)\mathbf{E}(x,y)_m.$$

(2.70)

where the subscript on the curl operator indicates that it is taken over the transverse field components only. The assumption made in Eq. (2.69) is that the perturbation is small such that the coefficient approaches unity and the projection of the electric field need not be separated into transverse and longitudinal components (it is also valid for an arbitrary perturbation in the case that the z-components of the fields are negligible). Notably, the coupled-mode equations themselves are not limited to the case of small perturbations if this approximation is not made.

Employing the normalization conditions of Eqs. (2.45) and (2.54), it is possible to simplify Eq. (2.69) even further:

$$\frac{dA_l(z)}{dz} = \sum_m -\frac{i\omega}{2} A_m(z)\exp\left[i(\beta_l - \beta_m)z\right]\frac{\int_{-\infty}^{\infty}\int_{-\infty}^{\infty}\Delta\varepsilon\,\mathbf{E}_m\cdot\mathbf{E}_l^{*}\,dxdy}{\int_{-\infty}^{\infty}\int_{-\infty}^{\infty}\mathbf{E}_l^{*}\times\mathbf{H}_l\cdot\mathbf{n}_z\,dxdy}$$

$$= \sum_m -\frac{i\omega}{2}\frac{\beta_l}{|\beta_l|} A_m(z)\exp\left[i(\beta_l - \beta_m)z\right]\frac{\int_{-\infty}^{\infty}\int_{-\infty}^{\infty}\Delta\varepsilon\,\mathbf{E}_m\cdot\mathbf{E}_l^{*}\,dxdy}{\frac{v_l}{2}\int_{-\infty}^{\infty}\int_{-\infty}^{\infty}\varepsilon\,\mathbf{E}_l\cdot\mathbf{E}_l^{*}\,dxdy}. \tag{2.71}$$

The system of differential equations of Eq. (2.71) is a description of the coupling of waveguide modes that occurs due to an arbitrary perturbation of the permittivity. The same reasoning can be easily modified to include perturbations of the permeability (alone or in conjunction with the permittivity), or be couched in terms of the magnetic field.

2.5.3. Bragg Reflection

The phenomenon of Bragg reflection arises when a periodic perturbation causes coupling between a forward propagating mode and a backward propagating mode [3]. For a perturbation periodic in the z direction, the permittivity may be decomposed into a Fourier series:

$$\varepsilon(x,y)+\Delta\varepsilon(x,y,z)=\sum_k \varepsilon_k(x,y)\exp\left(-ik\frac{2\pi}{\Lambda}z\right)-i\delta, \tag{2.72}$$

$$\varepsilon(x,y)=\varepsilon_0(x,y), \tag{2.73}$$

$$\Delta\varepsilon(x,y,z)=\sum_{k\neq 0} \varepsilon_k(x,y)\exp\left(-ik\frac{2\pi}{\Lambda}z\right)-i\delta, \tag{2.74}$$

where Λ is the perturbation period, k is an integer, and δ is a component of the permittivity that is included to account for waveguide loss (or equivalently gain when the sign is reversed). Most physical sources of loss are adequately described by the inclusion of such a zero-order term [10]. Substituting Eq. (2.74) into the general mode coupling equations of Eq. (2.71) produces:

$$\frac{d}{dz}A_l(z)=-\frac{\beta_l}{|\beta_l|}\frac{\alpha_l}{2}A_l(z)-i\frac{\beta_l}{|\beta_l|}\sum_{k\neq 0}\sum_m \kappa_{klm}A_m(z)\exp\left[i\left(\beta_l-\beta_m-k\frac{2\pi}{\Lambda}\right)z\right], \tag{2.75}$$

$$\kappa_{klm} = \frac{\omega}{2} \frac{\int_{-\infty}^{\infty}\int_{-\infty}^{\infty} \varepsilon_k(x,y)\mathbf{E}_m(x,y)\cdot\mathbf{E}_l(x,y)^* dxdy}{\frac{v_l}{2}\int_{-\infty}^{\infty}\int_{-\infty}^{\infty} \varepsilon\,\mathbf{E}_l\cdot\mathbf{E}_l{}^* dxdy},$$

(2.76)

$$\alpha_l = \omega \frac{\int_{-\infty}^{\infty}\int_{-\infty}^{\infty} \delta(x,y)\mathbf{E}_l\cdot\mathbf{E}_l{}^* dxdy}{\frac{v_l}{2}\int_{-\infty}^{\infty}\int_{-\infty}^{\infty} \varepsilon\,\mathbf{E}_l\cdot\mathbf{E}_l{}^* dxdy},$$

(2.77)

where the coefficient κ_{klm} represents the amount of coupling that occurs between the l^{th} and m^{th} modes as a consequence of the k^{th} Fourier coefficient of the perturbation, and α_l is the linear power loss coefficient. Note that the loss coefficients may be used to phenomenologically express any source of linear loss (such as radiative scattering) and not simply absorption arising from an imaginary component of the permittivty. The equations are intentionally expressed independently of the sign of the propagation constant (through the ratio of it and its absolute value) to emphasize that the coupled mode equations take a different form depending on whether the interacting modes are co-propagating or counter-propagating. In principle, the differential equations of Eq. (2.75) couple the amplitude of each mode to every other mode. In practice, net transfer of amplitude usually only occurs between a pair of modes. The intuitive explanation for this is that the complex exponential terms are generally rapidly varying (and when the sign of the integral rapidly changes no net coupling occurs on average). Significant

coupling will only occur when the phase of the complex exponential vanishes, such that:

$$\beta_l - \beta_m - k\frac{2\pi}{\Lambda} \approx 0\,, \tag{2.78}$$

which is known as the phase matching condition.

In accordance with Eqs. (2.75) through (2.78), Bragg reflection between a forward propagating wave (with propagation constant β_f) phase matched to a backward propagating wave (with propagation constant $-\beta_b$) arising from the $\pm k^{\text{th}}$ Fourier coefficient of the perturbation is described by the following coupled mode equations:

$$\frac{d}{dz}A_f(z) = -i\kappa_{kfb}A_b(z)\exp(i\Delta\beta z) - \frac{\alpha_f}{2}A_f(z), \tag{2.79}$$

$$\frac{d}{dz}A_b(z) = i\kappa_{-kbf}A_f(z)\exp(-i\Delta\beta z) + \frac{\alpha_b}{2}A_b(z), \tag{2.80}$$

$$\Delta\beta = \beta_f - (-\beta_b) - k\frac{2\pi}{\Lambda}\,. \tag{2.81}$$

The following relationship exists between the coupling coefficients:

$$\kappa_{-kbf} = \kappa_{kfb}^{*},$$

(2.82)

which follows from combining the definition of the coupling coefficient of Eq. (2.76), the normalization condition of Eq. (2.54), and the simple relationship between Fourier coefficients of a real function described in the Appendix. To continue the solution it is convenient to perform the following variable substitution:

$$A_f(z)' = A_f(z)\exp\left(\frac{\alpha_f z}{2}\right),$$

(2.83)

$$A_b(z)' = A_b(z)\exp\left(\frac{-\alpha_b z}{2}\right).$$

(2.84)

When Eqs. (2.83) and (2.84) are applied to Eqs. (2.79) and (2.80), the relationship between the new variables becomes:

$$\frac{d}{dz}A_f(z)' = -i\kappa_{kfb}A_b(z)'\exp(i\Delta\beta' z),$$

(2.85)

$$\frac{d}{dz}A_b(z)' = i\kappa_{-kbf}A_f(z)'\exp(-i\Delta\beta' z).$$

(2.86)

$$\Delta\beta' = \Delta\beta - i\frac{\alpha_f + \alpha_b}{2}.$$

(2.87)

The fields may be decoupled by differentiating Eqs. (2.85) and (2.86) and substituting the initial equations back in:

$$\frac{d^2}{dz^2}A_f(z)' = i\Delta\beta'\frac{d}{dz}A_f(z)' + \kappa_{kfb}\kappa_{-kbf}A_f(z)',$$

(2.88)

$$\frac{d^2}{dz^2}A_b(z)' = -i\Delta\beta'\frac{d}{dz}A_b(z)' + \kappa_{-kbf}\kappa_{kfb}A_b(z)'.$$

(2.89)

The general solution of Eqs. (2.88) and (2.89) assumes the form:

$$A_f(z)' = \exp\left(\frac{i\Delta\beta' z}{2}\right)\left[C_1\exp(sz) + C_1\exp(-sz)\right],$$

(2.90)

$$A_b(z)' = \exp\left(\frac{-i\Delta\beta' z}{2}\right)\left[D_1\exp(sz) + D_1\exp(-sz)\right],$$

(2.91)

$$s = \sqrt{\kappa_{kfb}\kappa_{-kbf} - \left(\frac{\Delta\beta'}{2}\right)^2} = \sqrt{\kappa_{kfb}\kappa_{-kbf} - \left(\frac{\Delta\beta}{2} - i\frac{\alpha_f + \alpha_b}{4}\right)^2}.$$

(2.92)

where C_1, C_2, D_1, and D_2 are constants to be determined by the initial condition of the fields.

The reflected and transmitted fields for a wave approaching in the forward direction arising from a perturbation of length L_{DBR} may be determined by considering the following boundary conditions:

$$A_f(0)' = A_f(0)',$$

(2.93)

$$A_b(L_{DBR})' = 0.$$

(2.94)

Applying the boundary conditions of Eqs. (2.93) and (2.94), the general solutions of Eqs. (2.90) and (2.91) may be rewritten:

$$A_f(z)' = 2C_1 \exp\left(\frac{i\Delta\beta' z}{2}\right)\sinh(sz) + A_f(0)' \exp\left(\frac{i\Delta\beta' z}{2}\right)\exp(-sz),$$

(2.95)

$$A_b(z)' = 2D_1 \exp(sL_{DBR})\exp\left(\frac{-i\Delta\beta' z}{2}\right)\sinh[s(z - L_{DBR})].$$

(2.96)

Next, differentiate Eqs. (2.95) and (2.96) and substitute in Eqs. (2.85) and (2.86):

$$
\begin{aligned}
&i\Delta\beta' C_1 \exp\left(\frac{i\Delta\beta' z}{2}\right)\sinh(sz) \\
&+2sC_1 \exp\left(\frac{i\Delta\beta' z}{2}\right)\cosh(sz) \\
&+\left(\frac{i\Delta\beta'}{2}-s\right)A_f(0)' \exp\left(\frac{i\Delta\beta z}{2}\right)\exp(-sz) \\
&=-i\kappa_{kfb}A_b(z)' \exp\left(i\Delta\beta' z\right)
\end{aligned}
,
\tag{2.97}
$$

$$
\begin{aligned}
&-i\Delta\beta' D_1 \exp(sL_{DBR})\exp\left(\frac{-i\Delta\beta' z}{2}\right)\sinh[s(z-L_{DBR})] \\
&+2sD_1 \exp(sL_{DBR})\exp\left(\frac{-i\Delta\beta' z}{2}\right)\cosh[s(z-L_{DBR})] \\
&=i\kappa_{-kbf}A_f(z)' \exp(-i\Delta\beta z)
\end{aligned}
.
\tag{2.98}
$$

The remaining constants may be determined by applying the boundary conditions of Eqs. (2.93) and (2.94) to Eqs. (2.97) and (2.98):

$$
C_1 = \frac{\left(s-\frac{i\Delta\beta'}{2}\right)A_f(0)' \exp(-sz)}{i\Delta\beta' \sinh(sL_{DBR})+2s\cosh(sL_{DBR})},
\tag{2.99}
$$

$$D_1 = \frac{i\kappa_{-kbf} A_f(0)' \exp(-sL_{DBR})}{i\Delta\beta' \sinh(sL_{DBR}) + 2s\cosh(sL_{DBR})}.$$

(2.100)

The coefficients of reflection r_{DBR} and transmission t_{DBR} for fields approaching the perturbation in the forward direction may be determined by combining the coefficients of Eqs. (2.99) and (2.100) with the solutions of Eq. (2.95) and (2.96):

$$r_{DBR}^{f\to b} = \frac{A_b(0)}{A_f(0)} = \frac{A_b(0)'}{A_f(0)'} = \frac{-2i\kappa_{-kbf} \sinh(sL_{DBR})}{i\Delta\beta' \sinh(sL_{DBR}) + 2s\cosh(sL_{DBR})},$$

(2.101)

$$t_{DBR}^{f\to f} = \frac{A_f(L_{DBR})}{A_f(0)} = \frac{A_f(L_{DBR})' \exp\left(\frac{-\alpha_f L_{DBR}}{2}\right)}{A_f(0)'} = \frac{2s\exp\left(\frac{i\Delta\beta' L_{DBR}}{2}\right)\exp\left(\frac{-\alpha_f L_{DBR}}{2}\right)}{i\Delta\beta' \sinh(sL_{DBR}) + 2s\cosh(sL_{DBR})}.$$

(2.102)

In terms of the original variables Eqs. (2.101) and (2.102) become:

$$r_{DBR}^{f\to b} = \frac{-i\kappa_{-kbf} L_{DBR}}{\left(\frac{i\Delta\beta}{2} + \frac{\alpha_f + \alpha_b}{4}\right)L_{DBR} + \frac{sL_{DBR}}{\tanh(sL_{DBR})}},$$

(2.103)

$$t_{DBR}^{f\to f}=\frac{\dfrac{sL_{DBR}\exp\left[\left(\dfrac{i\Delta\beta}{2}+\dfrac{\alpha_b-\alpha_f}{4}\right)L_{DBR}\right]}{\sinh\left(sL_{DBR}\right)}}{\left(\dfrac{i\Delta\beta}{2}+\dfrac{\alpha_f+\alpha_b}{4}\right)L_{DBR}+\dfrac{sL_{DBR}}{\tanh\left(sL_{DBR}\right)}},$$

(2.104)

$$s=\sqrt{\kappa_{kfb}\kappa_{-kbf}-\left(\frac{\Delta\beta}{2}\right)^2+\frac{i\Delta\beta}{4}\left(\alpha_f+\alpha_b\right)+\left(\frac{\alpha_f+\alpha_b}{4}\right)^2}\ .$$

(2.105)

2.5.4. Spectral Characteristics of a Bragg Reflector

All Bragg reflectors display a number of important spectral characteristics. In the absence of loss, the points $\Delta\beta = \pm 2|\kappa_{kfb}\kappa_{-kbf}|^{1/2}$ give $s = 0$ in Eq. (2.105) and are conventionally defined as the edges of the stopband, although it is clear from Eq. (2.103) that the reflectance is nonzero at these points:

$$\lim_{s\to 0}\left(r_{DBR}^{f\to b}\right)\Big|_{\alpha_f,\alpha_b=0}=\frac{-i\kappa_{-kbf}L_{DBR}}{\lim\limits_{s\to 0}\dfrac{i\Delta\beta}{2}L_{DBR}+\lim\limits_{s\to 0}\dfrac{sL_{DBR}}{\tanh\left(sL_{DBR}\right)}}=\frac{-i\kappa_{-kbf}L_{DBR}}{iL_{DBR}\sqrt{\kappa_{kfb}\kappa_{-kbf}}+1}\neq 0\,.$$

(2.106)

This definition arises from the fact that the fields in a Bragg reflector may be viewed as a Bloch wave, and the Bloch wavenumber becomes imaginary at these points. However, true reflectance null points do exist. They occur at the points $sL_{DBR} = ni\pi$ for integers $n \neq 0$, since $\tanh(sL_{DBR}) = 0$ but $sL_{DBR} \neq 0$ and therefore the limit of $|sL_{DBR} / \tanh(sL_{DBR})| = \infty$. The corresponding values of $\Delta\beta$ follow directly from Eq. (2.105):

$$\Delta\beta_{null} = \pm 2\sqrt{\kappa_{kfb}\kappa_{-kbf} + \left(\frac{n\pi}{L_{DBR}}\right)^2} \,. \tag{2.107}$$

The maximum reflectance of a Bragg reflector occurs at the center of the stopband where $\Delta\beta = 0$. The maximum magnitude of the coefficient of reflection of a lossless Bragg reflector is:

$$\left|r_{DBR}^{f\to b}\right\|_{\Delta\beta,\alpha_f,\alpha_b=0} = \left|\tanh\left(L_{DBR}\sqrt{\kappa_{kfb}\kappa_{-kbf}}\right)\right| . \tag{2.108}$$

In the presence of loss these features are more or less retained [11]. The theoretical spectral response of a lossless Bragg reflector following Eqs. (2.103) and (2.104) for which $|\beta_f| = |\beta_b| = |\beta|$ (and therefore $|\kappa_{kfb}| = |\kappa_{kbf}| = |\kappa|$) is shown in Fig. 2.1.

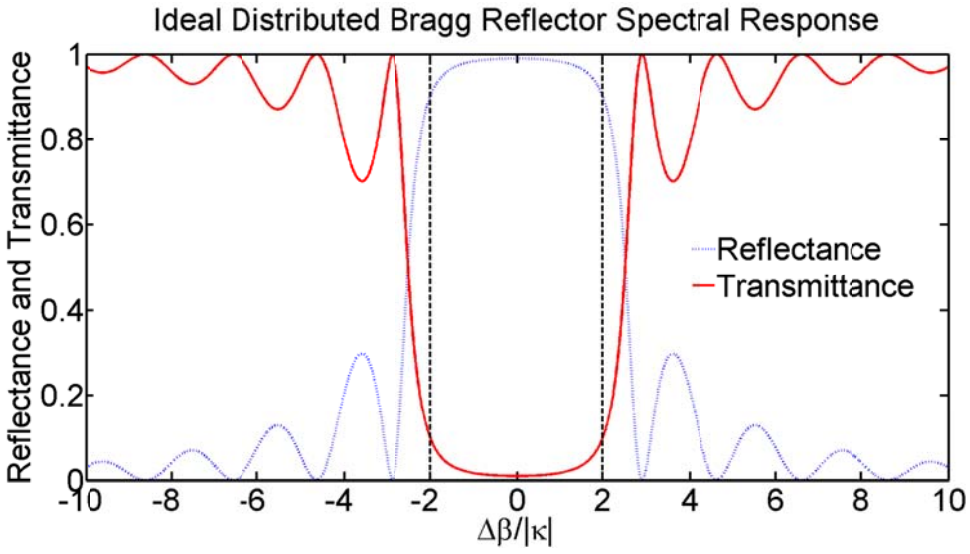

Fig. 2.1 Dependence of the response of an ideal Bragg reflector on spectral detuning. In this example $|\kappa|L_{DBR} = 3$. The dashed vertical lines indicate the conventional edge of the stopband.

2.6. Acknowledgements

This chapter, in part, is a reprint of "Characterization of waveguide loss using distributed Bragg reflectors" by A. Grieco, B. Slutsky, and Y. Fainman as it appears in Applied Physics B, volume 114, Springer, 2014. The dissertation author was the primary author of this paper.

3. Characterization of Distributed Bragg Reflectors

3.1. Motivation

Accurate estimation of the behavior of distributed Bragg reflectors is crucial to the development of a number of applications, including optical digital signal processing [12], optical switching [13], and nonlinear processes such as wave mixing [10]. Previous characterization attempts rely on curve fitting to the spectral response of photonic devices comprised of distributed Bragg reflectors over a broad spectral band [14]. To be accurate, a fitting process must account for the parameters of the Bragg reflector and resonant cavity separately, as well as account for the possibility of coupling loss due to mode mismatch of the periodic perturbation and that of the unperturbed waveguide in addition to the input and output coupling losses. Additionally, it must allow for the wavelength dependence of each of these parameters. The quantity of independent parameters has a significant detrimental effect on the robustness of the fit. To combat this proliferation of uncertainty a method of characerization was developed based on the linewidth comparison of Bragg reflectors in a resonant configuration. The method is independent of coupling efficiency, and the measurements are limited to a narrow spectral region.

3.2. Spectral Response of a Fabry-Pérot Resonator

A Fabry-Pérot resonator is comprised of a pair of partially reflective mirrors separated by some distance. When light is incident on the mirrors, certain wavelengths will constructively interfere upon reflection such that the optical field accumulates

between the mirrors. The spectral response of such a resonator may be calculated by summing the successive iterations of reflected and transmitted fields (known as Airy's formulas) [2]. The most generalization of this approach to a resonator composed of distributed Bragg reflectors described by Eqs. (2.103) and (2.104) is complicated because each mode must be accounted for. The coefficient of transmission t_{FP} of such a resonator is (in the complex field formalism):

$$t_{FP}^{f} = \begin{bmatrix} c_I^f t_{12}^{f\to f} c_M^f \sigma^f c_M^f t_{23}^{f\to f} c_O^f \\ + c_I^f t_{12}^{f\to f} c_M^f \sigma^f c_M^f \left(r_{23}^{f\to b} c_M^b \sigma^b c_M^b r_{21}^{b\to f} c_M^f \sigma^f c_M^f \right) t_{23}^{f\to f} c_O^f \\ + c_I^f t_{12}^{f\to f} c_M^f \sigma^f c_M^f \left(r_{23}^{f\to b} c_M^b \sigma^b c_M^b r_{21}^{b\to f} c_M^f \sigma^f c_M^f \right)^2 t_{23}^{f\to f} c_O^f \\ + \ldots \end{bmatrix}, \tag{3.1}$$

$$\sigma^{f,b} = \exp\left(i\beta^{f,b} L_c - \frac{\alpha_c^{f,b} L_c}{2} \right), \tag{3.2}$$

where c_I and c_O are the input and output amplitude coupling efficiencies, c_M is the amplitude coupling efficiency between the reflectors and the cavity. The σ term accounts for the phase shift and attenuation that a mode with propagation constant β and power loss (or gain) coefficient α_c incurs upon traversing a cavity of length L_c. The coefficients of transmission and reflection of the Bragg reflectors are represented by t_{ab} and r_{ab}, respectively, with the subscripts indicating order of occurrence and direction of incidence. Finally, superscripts indicate modal association. A conceptual illustration of such a resonator is produced in Fig. 3.1. In the general case the forward

and backward modes will have distinct transverse profiles, such that the field profile in the cavity will be more complex that what is ordinarily considered. The summation in Eq. (3.1) is an infinite geometric series and may be simplified as such:

$$t_{FP}^{f} = \frac{c_I^f t_{12}^{f\to f} c_M^f \sigma^f c_M^f t_{23}^{f\to f} c_O^f}{1 - r_{23}^{f\to b} c_M^b \sigma^b c_M^b r_{21}^{b\to f} c_M^f \sigma^f c_M^f}. \tag{3.3}$$

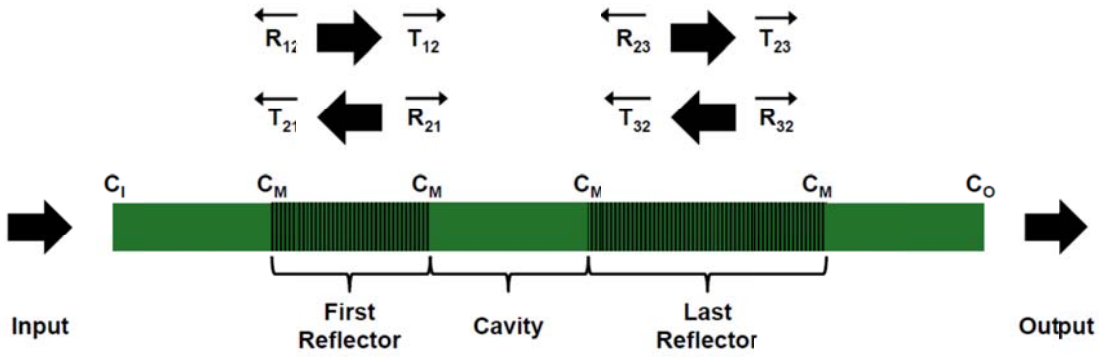

Fig. 3.1 Conceptual schematic of a Fabry-Pérot resonator comprised of a pair of distributed Bragg reflectors Arrows indicate direction of propagation, and labels correspond to their use in Eq. (3.1) and subsequent equations.

It is useful to consider the transmittance T_{FP} of the resonator explicitly in terms of the transmittance, reflectance and phase of the Bragg elements. The expression follows directly from Eq. (3.2) and Eq. (3.3):

$$T_{FP}^{f} = \left|t_{FP}^{f}\right|^2 = \frac{C_I^f T_{12}^{f\to f} \left(C_M^f\right)^2 \exp\left(-\alpha_c^f L_c\right) T_{23}^{f\to f} C_O^f}{\left|1 - \sqrt{R_{23}^{f\to b}} C_M^b \sqrt{R_{21}^{b\to f}} C_M^f \exp\left(-\frac{\alpha_c^b + \alpha_c^f}{2} L_c\right) \exp\left(i\phi_{Tot}\right)\right|^2}, \tag{3.4}$$

$$\phi_{Tot} = \left(\beta^b + \beta^f\right)L_c + \arg\left(r_{23}^{f\to b}\right) + \arg\left(r_{21}^{b\to f}\right),$$

(3.5)

where C_I and C_O are the input and output power coupling efficiencies, and C_M is the power coupling efficiency between the reflectors and the cavity. The ϕ_{Tot} term accounts for the total phase shift the field incurs upon traversing the cavity, with terms that include the phase shift upon reflection from the Bragg elements in addition to the linear phase. The transmittance and reflectance of the Bragg reflectors are represented by T_{ab} and R_{ab}, respectively, with the subscripts indicating order of occurrence and direction of incidence. As before, superscripts indicate modal association. The resonator transmittance of Eq. (3.4) may be written more conveniently in terms of trigonometric functions by expanding the denominator:

$$T_{FP}^f = \frac{C_I^f T_{12}^{f\to f}\left(C_M^f\right)^2 \exp\left(-\alpha_c^f L_c\right) T_{23}^{f\to f} C_O^f}{\left\{\begin{array}{l}\left[1-\sqrt{R_{23}^{f\to b}}C_M^b\sqrt{R_{21}^{b\to f}}C_M^f \exp\left(-\dfrac{\alpha_c^b+\alpha_c^f}{2}L_c\right)\right]^2 \\ +4\sqrt{R_{23}^{f\to b}}C_M^b\sqrt{R_{21}^{b\to f}}C_M^f \exp\left(-\dfrac{\alpha_c^b+\alpha_c^f}{2}L_c\right)\sin^2\left(\dfrac{\phi_{Tot}}{2}\right)\end{array}\right\}}.$$

(3.6)

It is possible to derive an explicit expression for the total phase shift ϕ_{Tot} from the resonator spectral response and the Bragg element parameters. To begin, eliminate the dependence on input and output coupling efficiency by normalizing Eq. (3.6) to the transmittance at resonance $T_{FP}|_{Res}$ (which occurs when ϕ_{Tot} is an integer multiple of 2π):

$$\frac{T_{FP}^{f}}{T_{FP}^{f}\Big|_{Res}}=\frac{\left[1-\sqrt{R_{23}^{f\to b}}C_{M}^{b}\sqrt{R_{21}^{b\to f}}C_{M}^{f}\exp\left(-\frac{\alpha_{c}^{b}+\alpha_{c}^{f}}{2}L_{c}\right)\right]^{2}}{\left\{\begin{array}{l}\left[1-\sqrt{R_{23}^{f\to b}}C_{M}^{b}\sqrt{R_{21}^{b\to f}}C_{M}^{f}\exp\left(-\frac{\alpha_{c}^{b}+\alpha_{c}^{f}}{2}L_{c}\right)\right]^{2}\\+4\sqrt{R_{23}^{f\to b}}C_{M}^{b}\sqrt{R_{21}^{b\to f}}C_{M}^{f}\exp\left(-\frac{\alpha_{c}^{b}+\alpha_{c}^{f}}{2}L_{c}\right)\sin^{2}\left(\frac{\phi_{Tot}}{2}\right)\end{array}\right\}}.$$

(3.7)

Next algebraically extract the desired phase term from Eq. (3.7):

$$\phi_{Tot}=\pm 2\arcsin\left\{\frac{\sqrt{\frac{T_{FP}^{f}\Big|_{Res}}{T_{FP}^{f}}-1}\left[1-\sqrt{R_{23}^{f\to b}}C_{M}^{b}\sqrt{R_{21}^{b\to f}}C_{M}^{f}\exp\left(-\frac{\alpha_{c}^{b}+\alpha_{c}^{f}}{2}L_{c}\right)\right]}{2\exp\left(-\frac{\alpha_{c}^{b}+\alpha_{c}^{f}}{4}L_{c}\right)\sqrt{\sqrt{R_{23}^{f\to b}}C_{M}^{b}\sqrt{R_{21}^{b\to f}}C_{M}^{f}}}\right\}.$$

(3.8)

From Eq. (3.8) the full width phase shift $\Delta\phi_{Tot}$ between points of equal transmittance (about a resonance peak, for example) is therefore:

$$\Delta\phi_{Tot}=4\arcsin\left\{\frac{\sqrt{\frac{T_{FP}^{f}\Big|_{Res}}{T_{FP}^{f}}-1}\left[1-\sqrt{R_{23}^{f\to b}}C_{M}^{b}\sqrt{R_{21}^{b\to f}}C_{M}^{f}\exp\left(-\frac{\alpha_{c}^{b}+\alpha_{c}^{f}}{2}L_{c}\right)\right]}{2\exp\left(-\frac{\alpha_{c}^{b}+\alpha_{c}^{f}}{4}L_{c}\right)\sqrt{\sqrt{R_{23}^{f\to b}}C_{M}^{b}\sqrt{R_{21}^{b\to f}}C_{M}^{f}}}\right\}.$$

(3.9)

The expression in Eq. (3.9) is significant in that it indicates the linewidth characteristics of a Fabry-Pérot resonator are determined entirely by the reflectance

characteristics of the mirror elements. In the appropriate limits, this can be exploited to characterize the parameters of a distributed Bragg reflector [15].

3.3. Phase Response of a Bragg Reflector

In the context of the expression for Fabry-Pérot linewidth of Eq. (3.9) it is useful to consider the behavior of phase upon reflection of a distributed Bragg reflector separately from the reflectance. It is possible to derive a convenient expression for the wavelength dependence of this phase near the center of the stopband [15]. To begin note that the phase is argument of the coefficient of reflection *r*, such that:

$$\frac{d\arg(r)}{d\Delta\beta} = \frac{d\,\mathrm{Im}[\ln(r)]}{d\Delta\beta}.$$

(3.10)

Next, substitute into Eq. (3.10) the coefficient of reflection of a Bragg reflector from Eq. (2.103):

$$\frac{d\arg(r)}{d\Delta\beta} = \frac{d}{d\Delta\beta}\mathrm{Im}\left\{\ln\left[-i\kappa_{-kbf}L_{DBR}\right]\right\} - \frac{d}{d\Delta\beta}\mathrm{Im}\left\{\ln\left[\left(\frac{i\Delta\beta}{2}+\frac{\alpha_f+\alpha_b}{4}\right)L_{DBR}+\frac{sL_{DBR}}{\tanh(sL_{DBR})}\right]\right\}.$$

(3.11)

The first term in Eq. (3.11) may be eliminated by noting that the coupling coefficient for the most common perturbations is a purely imaginary number (refer to the

Appendix for a discussion of this), and the remaining terms may be arranged as follows:

$$\frac{d\arg(r)}{d\Delta\beta} = -\mathrm{Im}\left\{\frac{d}{d\Delta\beta}\ln\left[\left(\frac{i\Delta\beta}{2}+\frac{\alpha_f+\alpha_b}{4}\right)L_{DBR}+\frac{sL_{DBR}}{\tanh(sL_{DBR})}\right]\right\}$$
$$= -\mathrm{Im}\left\{\frac{\frac{iL_{DBR}}{2}+\frac{d}{ds}\left[\frac{sL_{DBR}}{\tanh(sL_{DBR})}\right]\frac{ds}{d\Delta\beta}}{\left(\frac{i\Delta\beta}{2}+\frac{\alpha_f+\alpha_b}{4}\right)L_{DBR}+\frac{sL_{DBR}}{\tanh(sL_{DBR})}}\right\}. \tag{3.12}$$

Note that at the center of the stopband $\Delta\beta$ vanishes, and consequently s, $\tanh(s)$ and their derivatives are real numbers. Consequently Eq. (3.12) reduces to:

$$\left.\frac{d\arg(r)}{d\Delta\beta}\right|_{\Delta\beta=0} = -\mathrm{Im}\left\{\frac{\frac{iL_{DBR}}{2}+\frac{d}{ds}\left[\frac{sL_{DBR}}{\tanh(sL_{DBR})}\right]\frac{ds}{d\Delta\beta}}{\left(\frac{\alpha_f+\alpha_b}{4}\right)L_{DBR}+\frac{sL_{DBR}}{\tanh(sL_{DBR})}}\right\} = \frac{-\frac{1}{2}}{\left(\frac{\alpha_f+\alpha_b}{4}\right)+\frac{s}{\tanh(sL_{DBR})}}. \tag{3.13}$$

When written explicitly in terms of the fundamental parameters Eq. (3.13) becomes:

$$\left.\frac{d\arg(r)}{d\Delta\beta}\right|_{\Delta\beta=0} = -\frac{1}{2}\left[\left(\frac{\alpha_f+\alpha_b}{4}\right)+\frac{\sqrt{\kappa_{kfb}\kappa_{-kbf}+\left(\frac{\alpha_f+\alpha_b}{4}\right)^2}}{\tanh\left(L_{DBR}\sqrt{\kappa_{kfb}\kappa_{-kbf}+\left(\frac{\alpha_f+\alpha_b}{4}\right)^2}\right)}\right]^{-1}.$$

$$\approx \left.\frac{-1}{2\sqrt{\kappa_{kfb}\kappa_{-kbf}}}\right|_{\left(\frac{\alpha_f+\alpha_b}{4}\right)^2 << \kappa_{kfb}\kappa_{-kbf},\, L_{DBR}\sqrt{\kappa_{kfb}\kappa_{-kbf}} >> 1}$$

(3.14)

The theoretical phase response of a lossless Bragg reflector following Eqs. (2.103) and (2.104) for for which $|\beta_f| = |\beta_b| = |\beta|$ (and therefore $|\kappa_{kfb}| = |\kappa_{kbf}| = |\kappa|$) is shown in Fig. 3.2. The result is in good agreement with Eq. (3.14), specifically for the limiting case in which the hyperbolic tangent approaches unity.

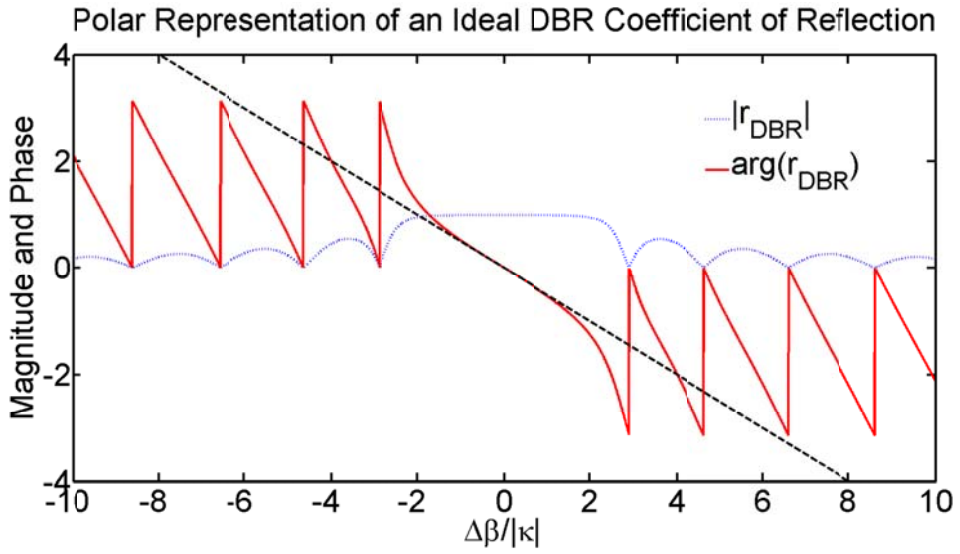

Fig. 3.2 Dependence of the phase response of an ideal Bragg reflector on spectral detuning. In this example $|\kappa|L_{DBR} = 3$. The dashed lines corresponds to the final limiting expression of Eq. (3.14).

3.4. Characterization of Loss Coefficients

Following coupled mode theory, the spectral response of a distributed Bragg reflector that couples arbitrary modes is in the most general sense determined by a pair of coupling coefficients, and a pair of loss coefficients. The coupling coefficients represent the strength with which the device transfers energy between the modes, and the loss coefficients represent how rapidly the energy of each mode is attenuated by the waveguide. In the special case that the Bragg reflector couples the forward propagating field of a mode to the backward propagating field of the same mode, the equations simplify such that the spectral response is determined by a single coupling coefficient and a single loss coefficient [15].

Consider a symmetrical Fabry-Pérot resonator composed of distributed Bragg reflectors that couples the forward propagating field of a mode to the backward propagating field of the same mode. In this case the relationship between linewidth and resonator phase shift of Eq. (3.9) reduces to:

$$\begin{aligned}\Delta\phi_{Tot} &= 2\beta L_c + 2\arg\left[r_{DBR}\left(\kappa_{DBR},\alpha_{DBR}\right)\right] \\ &= 4\arcsin\left\{\frac{\sqrt{\frac{T_{FP}\big|_{Res}}{T_{FP}}-1}\left[1-\left|r_{DBR}\left(\kappa_{DBR},\alpha_{DBR}\right)\right|^2 C_M^2\exp\left(-\alpha_c L_c\right)\right]}{2\exp\left(-\frac{\alpha_c}{2}L_c\right)\left|r_{DBR}\left(\kappa_{DBR},\alpha_{DBR}\right)\right|C_M}\right\},\end{aligned} \tag{3.15}$$

$$\kappa_{DBR} = \kappa_{-k(-f)f} = \kappa^*_{kf(-f)}, \tag{3.16}$$

where the dependence on coupling and loss coefficients is made explicit. It is possible to further simplify the linewidth and phase relationship by placing constraints on the resonator design. Specifically, consider a resonator in which the cavity is approximately a single perturbation period in length. In this situation, the loss from propagation through the cavity will be much less than the loss from propagation through the Bragg elements, which are many periods in length. Additionally, for such a short cavity the phase shift upon reflection from the Bragg elements will in general completely dominate the cavity phase shift. Finally, it is possible in general to design the resonator such that the loss due to mode mismatch is negligible. If the periodic perturbation is not so small that condition is not satisfied intrinsically, it is possible to adiabatically taper the transition from the Bragg elements to the cavity to eliminate the loss. Provided the taper is small compared to the total Bragg element length it will not otherwise impact the analysis (similar to the resonator cavity length). In these limits the expression of Eq. (3.15) reduces to:

$$\begin{aligned}\Delta\phi_{Tot} &\approx 2\arg\left[r_{DBR}\left(\kappa_{DBR},\alpha_{DBR}\right)\right] \\ &\approx 4\arcsin\left\{\frac{\sqrt{\frac{T_{FP}\big|_{Res}}{T_{FP}}-1}\left[1-\left|r_{DBR}\left(\kappa_{DBR},\alpha_{DBR}\right)\right|^2\right]}{2\left|r_{DBR}\left(\kappa_{DBR},\alpha_{DBR}\right)\right|}\right\}.\end{aligned} \tag{3.17}$$

Combining Eq. (3.17) with Eq. (3.14) and Eq. (2.103) allows the explicit expression of the linewidth in terms of the Bragg coefficients:

$$\Delta\phi_{Tot} \approx \left.\frac{d\arg(r)}{d\Delta\beta}\right|_{\Delta\beta=0} d\Delta\beta_{FW} \approx 2\arcsin\left\{\frac{\sqrt{\frac{T_{FP}|_{Res}}{T_{FP}}-1}\left[1-|r_{DBR}|^2_{\Delta\beta=0}\right]}{2|r_{DBR}|_{\Delta\beta=0}}\right\},$$

(3.18)

$$\left.\frac{d\arg(r)}{d\Delta\beta}\right|_{\Delta\beta=0} d\Delta\beta_{FW} = -\frac{1}{2}\left[\left(\frac{\alpha_f+\alpha_b}{4}\right)+\frac{\sqrt{\kappa_{kfb}\kappa_{-kbf}+\left(\frac{\alpha_f+\alpha_b}{4}\right)^2}}{\tanh\left(L_{DBR}\sqrt{\kappa_{kfb}\kappa_{-kbf}+\left(\frac{\alpha_f+\alpha_b}{4}\right)^2}\right)}\right]^{-1} d\Delta\beta_{FW},$$

(3.19)

$$|r_{DBR}|_{\Delta\beta=0} = \frac{L_{DBR}\sqrt{\kappa^*_{DBR}\kappa_{DBR}}}{\left(\frac{\alpha_{DBR}}{2}\right)L_{DBR}+\frac{L_{DBR}\sqrt{\kappa^*_{DBR}\kappa_{DBR}+\left(\frac{\alpha_{DBR}}{2}\right)^2}}{\tanh\left(L_{DBR}\sqrt{\kappa^*_{DBR}\kappa_{DBR}+\left(\frac{\alpha_{DBR}}{2}\right)^2}\right)}},$$

(3.20)

where $d\Delta\beta_{FW}$ is the full width change of the quantity $\Delta\beta$ (which is simply related to the resonance linewidth) at the points where the transmittance has the value of $T_{FP}/T_{FP}|_{Res}$ (for example $T_{FP}/T_{FP}|_{Res} = 1/2$ in the case of the full width at half maximum). It is possible to infer the values of κ_{DBR} and α_{DBR} from the comparison of linewidths of two symmetric resonators with different length Bragg elements from the expression in Eq.

(3.18), because they are formally equivalent to a system of two equations in two variables.

3.5. Characterization of Coupling Coefficients

The response of the most general type of distributed Bragg reflector is determined by four parameters: the coupling coefficients κ_{kfb} and κ_{-kbf}, and the loss coefficients α_f and α_b (here the subscripts f and b respectively indicate the forward and backward propagating modes). These parameters represent only three degrees of freedom, since the coupling coefficients are related to one another by Eq. (2.82). The loss coefficients may be determined according to the procedure described in the previous section. The remaining degree of freedom may be determined by measuring the linewidth of an appropriate Fabry-Pérot resonator (in a manner similar to the way that the loss is determined in the previous section).

Consider a symmetrical Fabry-Pérot resonator composed of distributed Bragg reflectors that couple two arbitrary forward and backward propagating modes. In this case the relationship between linewidth and resonator phase shift of Eq. (3.9) reduces to:

$$\Delta\phi_{Tot} = \left(\beta^b + \beta^f\right)L_c + \arg\left(r^{f\to b}\right) + \arg\left(r^{b\to f}\right)$$
$$= 4\arcsin\left\{\frac{\sqrt{\frac{T_{FP}^f\big|_{Res}}{T_{FP}^f} - 1}\left[1 - \sqrt{R^{f\to b}}C_M^b\sqrt{R^{b\to f}}C_M^f\exp\left(-\frac{\alpha_c^b + \alpha_c^f}{2}L_c\right)\right]}{2\exp\left(-\frac{\alpha_c^b + \alpha_c^f}{4}L_c\right)\sqrt{\sqrt{R^{f\to b}}C_M^b\sqrt{R^{b\to f}}C_M^f}}\right\}. \tag{3.21}$$

It is possible to further simplify the linewidth and phase relationship by placing constraints on the resonator design (identical to the constraints employed in the loss measurement of the previous section). Specifically, consider a resonator in which the cavity is approximately a single perturbation period in length. In this situation, the loss from propagation through the cavity will be much less than the loss from propagation through the Bragg elements, which are many periods in length. Additionally, for such a short cavity the phase shift upon reflection from the Bragg elements will in general completely dominate the cavity phase shift. Finally, it is possible in general to design the resonator such that the loss due to mode mismatch is negligible. If the periodic perturbation is not so small that condition is not satisfied intrinsically, it is possible to adiabatically taper the transition from the Bragg elements to the cavity to eliminate the loss. Provided the taper is small compared to the total Bragg element length it will not otherwise impact the analysis (similar to the resonator cavity length). In these limits the expression of Eq. (3.21) reduces to:

$$\Delta\phi_{Tot} \approx \arg\left(r_{DBR}^{f\to b}\right)+\arg\left(r_{DBR}^{b\to f}\right)$$
$$\approx 4\arcsin\left\{\frac{\sqrt{\frac{T_{FP}^{f}\big|_{Res}}{T_{FP}^{f}}-1}\left[1-\left|r_{DBR}^{f\to b}\right|\left|r_{DBR}^{b\to f}\right|\right]}{2\sqrt{\left|r_{DBR}^{f\to b}\right|\left|r_{DBR}^{b\to f}\right|}}\right\}.$$

(3.22)

Combining Eq. (3.22) with Eq. (3.14), Eq. (2.103) and Eq. (2.82) allows the explicit expression of the linewidth in terms of the Bragg coefficients:

$$\Delta\phi_{Tot}=\frac{d}{d\beta}\left[\arg\left(r_{DBR}^{f\to b}\right)+\arg\left(r_{DBR}^{b\to f}\right)\right]\Big|_{\Delta\beta=0}=4\arcsin\left\{\frac{\sqrt{\frac{T_{FP}^{f}\big|_{Res}}{T_{FP}^{f}}-1}\left[1-\left|r_{DBR}^{f\to b}\right|_{\Delta\beta=0}\left|r_{DBR}^{b\to f}\right|_{\Delta\beta=0}\right]}{2\sqrt{\left|r_{DBR}^{f\to b}\right|_{\Delta\beta=0}\left|r_{DBR}^{b\to f}\right|_{\Delta\beta=0}}}\right\},$$

(3.23)

$$\frac{d\arg\left(r_{DBR}^{m\to l}\right)}{d\beta}\Big|_{\Delta\beta=0}=-\left[\left(\frac{\alpha_m+\alpha_l}{4}\right)+\frac{\sqrt{\kappa_{kml}\kappa_{-klm}+\left(\frac{\alpha_m+\alpha_l}{4}\right)^2}}{\tanh\left(L_{DBR}\sqrt{\kappa_{kml}\kappa_{-klm}+\left(\frac{\alpha_m+\alpha_l}{4}\right)^2}\right)}\right]^{-1},$$

(3.24)

$$\left|r_{DBR}^{m\to l}\right| = \frac{L_{DBR}\sqrt{\kappa_{-klm}^{*}\kappa_{-klm}}}{\left(\frac{\alpha_m+\alpha_l}{4}\right)L_{DBR} + \frac{L_{DBR}\sqrt{\kappa_{kml}\kappa_{-klm}+\left(\frac{\alpha_m+\alpha_l}{4}\right)^2}}{\tanh\left(L_{DBR}\sqrt{\kappa_{kml}\kappa_{-klm}+\left(\frac{\alpha_m+\alpha_l}{4}\right)^2}\right)}}, \tag{3.25}$$

$$\kappa_{-kml} = \kappa_{klm}^{*}, \tag{3.26}$$

where $\Delta\beta_{FW}$ is again the full width of the resonance line at the points where the transmittance has the value of $T_{FP}/T_{FP}|_{Res}$ (for example $T_{FP}/T_{FP}|_{Res}$ = 1/2 in the case of the full width at half maximum). It is possible to infer the values of κ_{kfb} (or equivalently κ_{-kbf}) from the linewidth of a symmetric Bragg reflector Fabry-Pérot resonator using the expression in Eq. (3.23) because it is formally equivalent to a single equation in a single variable.

3.6. Experimental Considerations

The proposed and demonstrated method of characterization has a number of distinct advantages [15]. The only required measurements involve relative transmittance, which renders it independent of absolute coupling efficiency, and it employs resonant structures, which make it possible to accumulate a measurable quantity of loss within the smallest physical device footprint. In the context of nanoscale devices this eliminates a significant source of measurement uncertainty because the coupling efficiency is especially sensitive to fabrication uncertainty and

can be very difficult to characterize. Nanoscale devices are also prone to nonuniformity when they are not located within close proximity of one another. Finally, the method only involves measurement of a narrow spectral band. This minimizes any uncertainty that might arise from the wavelength dependence of the device parameters.

The limitations of the characterization method should be also be considered, however. It is necessary that the coupling efficiency and Bragg reflector parameters must not vary significantly with wavelength across the resonance, and that the coupling efficiency remain constant over time, otherwise error will be introduced into the measurement. The measurements are limited to a narrow bandwidth, so the measurement time and spectral sensitivity will be minimal. These requirements are trivially satisfied by most coupling mechanisms [16], [17], [18].

Attention must be given to the total operating power. While increasing Bragg reflector length will increase sensitivity to the coupling and loss coefficients, extremely high reflectance values can cause excessive power accumulation in the resonator and subsequent nonlinear behavior [19]. Additionally, if the transmitted power is small the measurement risks being contaminated by the noise floor of the experimental system. These problems can be avoided by appropriate consideration during the experimental design stage.

A more subtle potential source of error is the impedance mismatch between different sections of waveguide and at the couplers. Technically these constitute additional points of reflection, and a physical device is essentially a series of coupled

resonators. Should the impedance mismatch at these points be nontrivial the spectral response of the device would become very complex and the necessary linewidth measurements would be impossible. If present, this effect would be clearly visible since the desired spectral response is very simple. In general, these reflections can be minimized by adiabatically tapering the waveguide between transition sections.

Finally, the uncertainty and variation that is naturally associated with the fabrication process of a physical device can lead to unintended differences between the various structures required for the measurement. Nanoscale fabrication variation arises from numerous causes, including lithography distortion and wafer variation. Typically these are minimal for devices that are located in close proximity to one another. As such, proper consideration during the experimental design can minimize their influence.

3.7. Acknowledgements

This chapter, in part, is a reprint of "Characterization of Distributed Bragg Reflectors" by A. Grieco, and Y. Fainman as it appears in the Journal of Quantum Electronics, volume 50, Institute of Electrical and Electronics Engineers (IEEE), 2014. The dissertation author was the primary author of this paper.

4. Characterization of Waveguide Loss

4.1. Motivation

The accurate estimation of waveguide loss is critical to the design of integrated photonic devices, particularly nonlinear devices which can become unstable when operated at unanticipated power levels [10]. The most common methods of loss characterization become problematic when applied to low loss integrated waveguides. The cutback method [20] requires the fabrication of prohibitively long devices, and separation of coupling loss from waveguide loss. Resonant methods [21] ameliorate the device length requirement and are independent of coupling, but require bending of the waveguide. Waveguide bending introduces excess loss which in itself must be accounted for, and also distorts the mode profile which alters its susceptibility to other sources of loss. To avoid these sources of uncertainty a method of loss characterization was developed based on the comparison of the spectra response of devices comprised of Bragg reflectors. The method is independent of coupling efficiency, requires a small device footprint, does not require the introduction of bending into the device, and does not confuse loss in the Bragg reflectors with waveguide loss.

4.2. Reflectance Minima of a Bragg Reflector

A method of waveguide loss characterization based on the comparison of distributed Bragg reflector Fabry-Pérot resonators has been demonstrated [11]. This characterization method relies on the existence of reflectance null points in the

response of the Bragg reflector to normalize the transmittance spectra of the resonators involved. When loss is included in the Bragg reflector equations, the reflectance does not truly vanish at the minima, but remains negligibly small. To demonstrate this, consider the parameter *s* described by Eq. (2.105) at one of the null points described by Eq. (2.107). Neglecting the terms that are second order in the loss coefficients, the product sL_{DBR} at becomes:

$$sL_{DBR} \approx \sqrt{-(n\pi)^2 + \frac{i\Delta\beta_{null}}{4}(\alpha_f + \alpha_b)L_{DBR}^2}\ . \tag{4.1}$$

Next take the Taylor series of Eq. (4.1), again neglecting terms that are second order in the loss coefficients:

$$sL_{DBR} \approx ni\pi\left[1 - \frac{i\Delta\beta_{null}}{8(n\pi)^2}(\alpha_f + \alpha_b)L_{DBR}^2\right] = ni\pi + \frac{\Delta\beta_{null}}{8n\pi}(\alpha_f + \alpha_b)L_{DBR}^2\ . \tag{4.2}$$

Next apply the approximation of Eq. (4.2) to simplify the denominator of the coefficient of reflection expressed in Eq. (2.103) that contains a hyperbolic tangent:

$$\frac{sL_{DBR}}{\tanh(sL_{DBR})} \approx \frac{ni\pi}{\tanh\left(ni\pi + \frac{\Delta\beta_{null}}{8n\pi}(\alpha_f + \alpha_b)L_{DBR}^2\right)}\ . \tag{4.3}$$

The neglect of the term in the numerator containing waveguide loss coefficients is justified on the grounds that since $|ni\pi / \tanh(ni\pi)| = \infty$, for a small perturbing term Δ

then $|(ni\pi + \Delta) / \tanh(ni\pi + \Delta)| \approx \infty \approx |ni\pi / \tanh(ni\pi + \Delta)|$. Taking the hyperbolic tangent of Eq. (4.3) to first order in the loss coefficients and substituting in the expression for $\Delta\beta_{null}$ of Eq. (2.107) results in:

$$\frac{sL_{DBR}}{\tanh\left(sL_{DBR}\right)} \approx \frac{ni\pi}{\frac{\Delta\beta_{null}}{8n\pi}\left(\alpha_f + \alpha_b\right)L_{DBR}^2} = \frac{\pm 4i\left(n\pi\right)^2}{\left(\alpha_f + \alpha_b\right)L_{DBR}^2\sqrt{\kappa_{kfb}\kappa_{-kbf} + \left(\frac{n\pi}{L_{DBR}}\right)^2}}. \tag{4.4}$$

Substituting the approximation of Eq. (4.4) and Eq. (2.107) into the expression for the coefficient of reflection Eq. (2.103) and neglecting terms that are second order in the loss coefficients results in the approximation:

$$\left|r_{DBR}^{f\to b}\right|_{\Delta\beta_{null}} \approx \frac{\left|\kappa_{-kbf}\right|L_{DBR}\left(\alpha_f + \alpha_b\right)L_{DBR}\sqrt{\kappa_{kfb}\kappa_{-kbf}L_{DBR}^2 + \left(n\pi\right)^2}}{4\left(n\pi\right)^2}. \tag{4.5}$$

The periodic perturbation of the Bragg reflector is an engineered structure, and from inspection of Eq. (4.5) it is clear that it is generally possible to design the Bragg reflector such that the maximum reflectance is large and the reflectance at the null points is vanishingly small. Any of the null points $n = 1, 2, 3$ ... may be used for the purpose of normalization. Higher order null points reduce the minimum reflectance but move the reference wavelength farther from the Bragg reflector stopband, which may cause the wavelength dependence of the parameters to introduce error during the characterization process.

4.3. Characterization of the Loss Coefficient

The loss of an unperturbed waveguide is not in general the same as the loss in a perturbed structure, such as a distributed Bragg reflector. This may be intuitively understood from the fact that the transverse mode profile varies in each structure, and therefore the overlap of the mode with the sources of loss will also vary. Each waveguide mode is associated with a distinct loss coefficient, and the most precise method of loss characterization will involve the measurement of one mode at a time. For this reason it is most expedient to utilize Bragg reflectors that couple the forward and backward propagating fields of a single mode. In accordance with Eqs. (3.4) and (3.5) the transmittance of such a Bragg reflector Fabry-Pérot resonator is:

$$T_{FP} = \frac{C_I T_{12} C_M^2 \exp(-\alpha_c L_c) T_{23} C_O}{\left|1 - \sqrt{R_{23}} C_M^2 \sqrt{R_{21}} \exp(-\alpha_c L_c) \mathrm{Re}\left[\exp(i\phi_{Tot})\right]\right|^2}, \tag{4.6}$$

$$\phi_{Tot} = 2\beta L_c + \arg(r_{23}) + \arg(r_{21}). \tag{4.7}$$

First apply Eq. (4.6) to the case of a resonator with a short cavity approximately one perturbation period in length. In this arrangement the loss of the cavity will be negligible compared to the loss of the Bragg reflectors since the reflectors are many periods long. Consequently the resonator transmittance of Eq. (4.6) reduces to:

$$T_{FP}^{short} = \frac{C_I T_{12} C_M^2 T_{23} C_O}{\left|1 - \sqrt{R_{23}} C_M^2 \sqrt{R_{21}}\,\mathrm{Re}\left[\exp\left(i\phi_{Tot}\right)\right]\right|^2}.$$

(4.8)

Two important observations follow from the transmittance of Eq. (4.8). First, the transmittance at the reflectance null points is:

$$T_{FP}^{short}\Big|_{\beta_{null}} = C_I T_{12}\Big|_{\beta_{null}} C_M^2 T_{23}\Big|_{\beta_{null}} C_O.$$

(4.9)

Second, the transmittance at the cavity resonance is:

$$T_{FP}^{short}\Big|_{\beta_{res}^{short}} = \frac{C_I T_{12}\Big|_{\beta_{res}^{short}} C_M^2 T_{23}\Big|_{\beta_{res}^{short}} C_O}{\left|1 - \sqrt{R_{23}\Big|_{\beta_{res}^{short}}} C_M^2 \sqrt{R_{21}\Big|_{\beta_{res}^{short}}}\right|^2}.$$

(4.10)

The reflectances and mode coupling loss coefficient can be separated from the transmittances by dividing Eq. (4.10) by Eq. (4.9) and extracting the desired term:

$$\sqrt{R_{23}\Big|_{\beta_{res}^{short}}} C_M^2 \sqrt{R_{21}\Big|_{\beta_{res}^{short}}} = 1 - \sqrt{\frac{T_{12}\Big|_{\beta_{res}^{short}}}{T_{12}\Big|_{\beta_{null}}}} \sqrt{\frac{T_{23}\Big|_{\beta_{res}^{short}}}{T_{23}\Big|_{\beta_{null}}}} \sqrt{\frac{T_{FP}^{short}\Big|_{\beta_{null}}}{T_{FP}^{short}\Big|_{\beta_{res}^{short}}}}.$$

(4.11)

The relationship of Eq. (4.11) gives the product of mode coupling loss and reflectances at the resonance of the short cavity in terms of various power transmittance ratios. These power transmittance ratios can be obtained separately from

the measured transmittance spectrum of the individual Bragg reflector elements and the short resonance cavity. These ratio measurements are independent of any coupling loss (whether from mode coupling or input and output coupling).

With the knowledge of the mode coupling loss and reflectances from Eq. (4.11), it is possible to infer waveguide loss from a resonator with a long resonant cavity. In such an arrangement, the cavity loss can no longer be neglected. From Eq. (4.6) the resonator transmittance at the null points is thus:

$$T_{FP}^{long}\Big|_{\beta_{null}} = C_I T_{12}\big|_{\beta_{null}} C_M^2 \exp(-\alpha_c L_c) T_{23}\big|_{\beta_{null}} C_O .$$

(4.12)

Likewise, the transmittance at the cavity resonance is:

$$T_{FP}^{long}\Big|_{\beta_{res}^{long}} = \frac{C_I T_{12}\big|_{\beta_{res}^{long}} C_M^2 \exp(-\alpha_c L_c) T_{23}\big|_{\beta_{res}^{long}} C_O}{\left|1-\sqrt{R_{23}\big|_{\beta_{res}^{long}}} C_M^2 \sqrt{R_{21}\big|_{\beta_{res}^{long}}} \exp(-\alpha_c L_c)\right|^2} .$$

(4.13)

The exponential containing the loss coefficient can be obtained by dividing Eq. (4.13) by Eq. (4.12) and extracting the desired term:

$$\exp(-\alpha_c L_c) = \frac{1-\sqrt{\frac{T_{12}\big|_{\beta_{res}^{long}}}{T_{12}\big|_{\beta_{null}}}}\sqrt{\frac{T_{23}\big|_{\beta_{res}^{long}}}{T_{23}\big|_{\beta_{null}}}}\sqrt{\frac{T_{FP}^{long}\Big|_{\beta_{null}}}{T_{FP}^{long}\Big|_{\beta_{res}^{long}}}}}{\sqrt{R_{23}\big|_{\beta_{res}^{long}}} C_M^2 \sqrt{R_{21}\big|_{\beta_{res}^{long}}}} .$$

(4.14)

It is generally possible to choose the long cavity length so that one of its resonances coincides with one of the resonances of the short cavity. For example, if both cavities lengths are integer multiples of the perturbation period each cavity will have a resonance at the exact center of the Bragg reflector stopband. For such coincident resonances, the product of mode coupling loss and reflectances from the denominator of Eq. (4.14) is known from Eq. (4.11). The loss factor is the readily solved from Eq. (4.14):

$$\exp\left(-\alpha_c L_c\right) = \frac{1 - \sqrt{\frac{T_{12}\big|_{\beta_{res}}}{T_{12}\big|_{\beta_{null}}}}\sqrt{\frac{T_{23}\big|_{\beta_{res}}}{T_{23}\big|_{\beta_{null}}}}\sqrt{\frac{T_{FP}^{long}\big|_{\beta_{null}}}{T_{FP}^{long}\big|_{\beta_{res}}}}}{1 - \sqrt{\frac{T_{12}\big|_{\beta_{res}}}{T_{12}\big|_{\beta_{null}}}}\sqrt{\frac{T_{23}\big|_{\beta_{res}}}{T_{23}\big|_{\beta_{null}}}}\sqrt{\frac{T_{FP}^{short}\big|_{\beta_{null}}}{T_{FP}^{short}\big|_{\beta_{res}}}}}. \tag{4.15}$$

The waveguide loss may therefore be determined by measuring the transmittances of the appropriate assemblies of Bragg reflectors. Placing the resonance near the center of the stopband is especially advantageous because the properties of the Bragg reflector at band center are less sensitive to frequency errors.

4.4. Experimental Considerations

The proposed and demonstrated method of waveguide loss characterization has a number of advantages [11]. Similar to the method of the previous section, the only required measurements involve relative transmittance, which renders it independent of absolute coupling efficiency, and it employs resonant structures, which make it

possible to accumulate a measurable quantity of loss within the smallest physical device footprint. As before, in the context of nanoscale devices this eliminates a significant source of measurement uncertainty because the coupling efficiency is especially sensitive to fabrication uncertainty and can be very difficult to characterize. Likewise, nanoscale devices are also prone to nonuniformity when they are not located within close proximity of one another. Additionally, this method is not degraded by waveguide dispersion, which only serves to shift the relative position of the relevant spectral features (and does not affect their magnitude, which is the critical measurement parameter).

The limitations of the characterization method are also similar to that of the previous section. It is necessary that the absolute coupling efficiency does not drift over the measurement time and that the coupling efficiency by identical at the null and resonance measurement points, otherwise error will be introduced into the power ratio measurements. It is also necessary that the waveguide loss be identical at the null and resonance measurement points (although it is not necessary that the Bragg reflector loss be identical at these points). In practice this condition will be met in most waveguides, except near points of material absorption lines.

The error in the proposed loss characterization scheme may be broadly categorized into three main sources. The first source is the noise floor of the measurement system, which can become significant if the Bragg elements have high reflectance and the absolute transmittance at the center of the stopband is low. In such a situation it will be impossible to accurately calculate the transmission ratios used to

determine Bragg reflectance and power loss. This problem can typically be avoided during the experimental design phase, although the noise floor can be avoided in principle by operating at higher power (although this can cause the onset of nonlinear effects which are equally problematic [19]).

The second source of error is the impedance mismatch between different sections of waveguide and at the couplers. These constitute additional points of reflection, and if the effect is significant the physical device becomes a series of coupled resonators with a complicated spectral response. Generally, these reflections can be minimized by adiabatically tapering the waveguide between transition sections. For devices that employ tapered couplers [16] the reflections can be further reduced by creating the access facets at an angle to the waveguides (this could complicate fabrication and reduce coupling efficiency). Increasing the distance between the points of reflection will also mitigate this effect by damping the unintentional resonators (although this will increase the total device footprint).

The third source of error is a result of uncertainty in the fabrication processes, which leads to unintended differences between the resonator structures. Typically this uncertainty is relatively small, but if the propagation loss incurred over the cavity length is also relatively small, the fabrication could compromise the measurement. Nanoscale fabrication variation arises from numerous causes, including lithography distortion and wafer variation, and consequently it will increase with larger device separation and longer exposure times. These errors may also alter the optical path lengths of the resonator cavities and shift the position of the measurement points.

However, the change in Bragg reflector parameters at the center of the stopband is very small, so a device engineered with a broad stopband will be resilient. In the worst-case scenario, multiple devices may be fabricated and the best matching ones used for the measurement.

4.5. Acknowledgements

This chapter, in part, is a reprint of "Characterization of waveguide loss using distributed Bragg reflectors" by A. Grieco, B. Slutsky, and Y. Fainman as it appears in Applied Physics B, volume 114, Springer, 2014. The dissertation author was the primary author of this paper.

5. Optical Bistability in Bragg Reflector Resonators

5.1. Motivation

Bistability is a phenomena that can occur in photonic devices with a nonlinear optical response [19]. In the bistable regime of a resonant cavity the output power of the device is not uniquely determined by the input power because multiple powers within the cavity can satisfy the resonant condition. Due to this peculiarity the steady state response of a bistable Fabry-Pérot resonator must be modeled by expressing the input power of the device as a function of the output power. Bistable devices can serve as a foundation for optical signal processing because they display both nonlinearity and hysteresis, which allows for the realization of photonic circuitry with functions including switching, memory, logic, and modulation [22]. It is important to understand this behavior, because its unwanted manifestation can interfere with the intended function of a photonic device.

5.2. Nonlinear Phase Modulation

To begin the analysis, it is necessary to determine the effect that nonlinearity has upon the phase of a field propagating within a waveguide. The effect of optical nonlinearities may be incorporated by expressing the electric polarization of Eq. (2.5) as a Taylor series in terms of the electric field:

$$\mathbf{P} = \varepsilon_0\left(\chi_{\mathbf{E}}^{(1)}\vdots\mathbf{E} + \chi_{\mathbf{E}}^{(2)}\vdots\mathbf{EE} + \chi_{\mathbf{E}}^{(3)}\vdots\mathbf{EEE} + \ldots\right), \tag{5.1}$$

where the χ tensors represent the nonlinear susceptibility of the material. In a waveguide the maximum nonlinear effect is achieved when all the power is confined to a single mode. In this situation a field with both co-propagating and counter-propagating components assumes the form:

$$\begin{aligned}\mathbf{E}(x,y,z,t) &= \mathrm{Re}\{A_F(z)\mathbf{E}(x,y)\exp[i(\omega t-\beta z)]+A_B(z)\mathbf{E}(x,y)\exp[i(\omega t+\beta z)]\}\\ &= \frac{1}{2}\{A_F(z)\mathbf{E}(x,y)\exp[i(\omega t-\beta z)]+A_B(z)\mathbf{E}(x,y)\exp[i(\omega t+\beta z)]+\text{c.c.}\}\end{aligned}$$

(5.2)

where c.c. indicates the complex conjugate of the preceding terms. Consider a material in which only the third order nonlinearity is significant. The electric polarization of such a material may be obtained by substituting Eq. (5.2) into Eq. (5.1) and neglecting the rapidly varying terms:

$$\mathbf{P} = \mathbf{P}_{Linear} + \mathbf{P}^{F}_{Nonlinear} + \mathbf{P}^{B}_{Nonlinear},$$

(5.3)

$$\mathbf{P}_{Linear} = \varepsilon_0\, \chi^{(1)}_{\mathbf{E}} \vdots \mathbf{E},$$

(5.4)

$$\mathbf{P}^{F}_{Nonlinear} = \varepsilon_0\, \chi^{(3)}_{\mathbf{E}} \vdots \mathbf{E}\mathbf{E}\mathbf{E}\frac{1}{2}\left\{\left[\frac{3}{2}\left|A_B(z)\right|^2 A_F(z)+\frac{3}{4}\left|A_F(z)\right|^2 A_F(z)\right]\exp[i(\omega t-\beta z)]+\text{c.c.}\right\},$$

(5.5)

$$\mathbf{P}^{B}_{Nonlinear} = \varepsilon_0 \, \chi^{(3)}_{\mathbf{E}} \vdots \mathbf{EEE} \frac{1}{2} \left\{ \left[\frac{3}{2} \left| A_F(z) \right|^2 A_B(z) + \frac{3}{4} \left| A_B(z) \right|^2 A_B(z) \right] \exp\left[i(\omega t + \beta z) \right] + \text{c.c.} \right\}.$$

(5.6)

If we treat the nonlinearity as a perturbation we may apply the coupled-mode theory developed previously by substitution of Eqs. (5.2) and (5.3) in place of Eqs. (2.66) and (2.67). The only minor difference is that additional forward and backward propagating fields occur in the subsequent equations. Otherwise, the separate treatment of each field proceeds exactly as before, and most of the additional terms are discarded as rapidly varying since no special phase matching condition is assumed. Applying the coupled-mode machinery produces the following equations governing amplitude evolution:

$$\frac{d}{dz} A_F(z) = -i\gamma \left[\left| A_F(z) \right|^2 + 2 \left| A_B(z) \right|^2 \right] A_F(z) - \frac{\alpha}{2} A_F(z),$$

(5.7)

$$\frac{d}{dz} A_B(z) = i\gamma \left[\left| A_B(z) \right|^2 + 2 \left| A_F(z) \right|^2 \right] A_B(z) + \frac{\alpha}{2} A_F(z),$$

(5.8)

$$\gamma = \sum_m \frac{3\omega}{8} \frac{\int_{-\infty}^{\infty} \int_{-\infty}^{\infty} \varepsilon(x,y) \chi^{(3)}_{\mathbf{E}} \vdots \mathbf{EEE} \cdot \mathbf{E}_l^{\,*} \, dxdy}{\frac{v_l}{2} \int_{-\infty}^{\infty} \int_{-\infty}^{\infty} \varepsilon \, \mathbf{E}_l \cdot \mathbf{E}_l^{\,*} \, dxdy}.$$

(5.9)

A loss coefficient has also been included in the perturbation for completeness, in the same manner as Eqs. (2.74) and (2.77).

A great deal of information about the behavior of the fields can be obtained by rewriting Eqs. (5.7) and (5.8) in terms of absolute power and phase such that:

$$A(z) = \sqrt{P(z)}\exp[i\phi(z)].$$

(5.10)

By inspection of Eqs. (5.10) the derivatives of the absolute power and phase must obey the following relationships:

$$\frac{d}{dz}P(z) = A(z)\frac{d}{dz}A(z)^* + A(z)^*\frac{d}{dz}A(z) = 2\,\mathrm{Re}\left[A(z)^*\frac{d}{dz}A(z)\right],$$

(5.11)

$$\frac{d}{dz}\phi(z) = \frac{d}{dz}\mathrm{Im}\{\ln[A(z)]\} = \mathrm{Im}\left\{\frac{1}{A(z)}\frac{d}{dz}A(z)\right\}.$$

(5.12)

Application of Eqs. (5.11) and (5.12) to Eqs. (5.7) and (5.8) produces the following relationships:

$$\frac{d}{dz}P_F(z) = -\alpha P_{F,B}(z),$$

(5.13)

$$\frac{d}{dz}P_B(z)=\alpha P_B(z),$$

(5.14)

$$\frac{d}{dz}\phi_F(z)=-\gamma\left[P_F(z)+2P_B(z)\right].$$

(5.15)

$$\frac{d}{dz}\phi_B(z)=\gamma\left[P_B(z)+2P_F(z)\right].$$

(5.16)

The solution of Eqs. (5.13) through (5.16) is trivial:

$$P_F(z)=P_F(0)\exp(-\alpha z),$$

(5.17)

$$P_B(z)=P_F(0)\exp(\alpha z)=P_B(L)\exp(-\alpha L)\exp(\alpha z),$$

(5.18)

$$\phi_F(L)=\int_0^L\frac{d}{dz}\phi_F(z)dz=-\gamma\left[P_F(0)+2P_B(L)\right]\left[\frac{1-\exp(-\alpha L)}{\alpha}\right],$$

(5.19)

$$\phi_B(L)=\int_0^L\frac{d}{dz}\phi_B(z)dz=\gamma\left[P_B(L)+2P_F(0)\right]\left[\frac{1-\exp(-\alpha L)}{\alpha}\right].$$

(5.20)

It is clear from Eqs. (5.17) through (5.20) that the nonlinearity only to modulates the phase of the fields and does not transfer power between them.

5.3. Steady State Bistability

Following Eqs. (3.1) and (3.2), the response of a nonlinear resonator that obeys Eqs. (5.15) and (5.16) is:

$$T_{FP} = \frac{C_I T_{12} C_M^2 \exp(-\alpha_c L_c) T_{23} C_O}{\left|1 - \sqrt{R_{23}} C_M^2 \sqrt{R_{21}} \exp(-\alpha_c L_c) \exp(i\phi_{Tot})\right|^2},$$

(5.21)

$$\phi_{Tot} = \phi_{Linear} + \phi_{Nonlinear},$$

(5.22)

$$\phi_{Linear} = 2\beta L_c + \arg(r_{23}) + \arg(r_{21}),$$

(5.23)

$$\phi_{Nonlinear} = \phi_B(L_c) - \phi_F(L_c).$$

(5.24)

Since the output power of a bistable Fabry-Pérot resonator is not unique, the steady state response of the device must be modeled by expressing the input power of the device as a function of the output power. For the proper description it is necessary to couch the power within the resonator in terms of the output power. This may be done by considering the power within the cavity as being divided between two counter propagating waves such that [2]:

$$P_O = T_{FP} P_I \rightarrow P_I = \frac{P_O}{T_{FP}},$$

(5.25)

$$P_O = P_F(0)\exp(-\alpha_c L_c) C_M^2 T_{23} C_O \rightarrow P_F(0) = \frac{P_O \exp(\alpha_c L_c)}{C_M^2 T_{23} C_O},$$

(5.26)

$$P_B(L_c) = R_{23} C_M^2 P_F(L_c) = R_{23} C_M^2 P_F(0)\exp(-\alpha_c L_c) \rightarrow P_B(L_c) = \frac{P_O R_{23}}{T_{23} C_O},$$

(5.27)

where P_I is the input power measured prior to the input coupling junction C_I, and P_O is the output power measured following the output coupling junction C_O. Combining Eqs. (5.25) through (5.27) with Eqs. (5.21) through (5.24) leads to the desired implicit description of bistability:

$$P_I = P_O \frac{\left|1 - \sqrt{R_{23}} C_M^2 \sqrt{R_{21}} \exp(-\alpha_c L_c)\exp(i\phi_{Tot})\right|^2}{C_I T_{12} C_M^2 \exp(-\alpha_c L_c) T_{23} C_O},$$

(5.28)

$$\phi_{Tot} = 2\beta L_c + \arg(r_{23}) + \arg(r_{21}) + 3\gamma P_O \left[\frac{1 - \exp(-\alpha_c L_c)}{\alpha_c}\right]\left[\frac{\exp(\alpha_c L_c) + C_M^2 R_{23}}{C_M^2 T_{23} C_O}\right].$$

(5.29)

The bistable transfer function of a lossless symmetric resonator at a point of linear resonance following Eqs. (5.28) and (5.29) is shown in Fig. 5.1. The resonator can

only approach the bistable regime from a low or high power state, so the intermediate power in the figure is not physical. This analysis neglects the time dependent behavior of the bistable system, in which it is possible for the resonator to oscillate between the bistable states (either with regularity or chaotically). The time dependent behavior of the system may be evaluated using linear stability analysis [10].

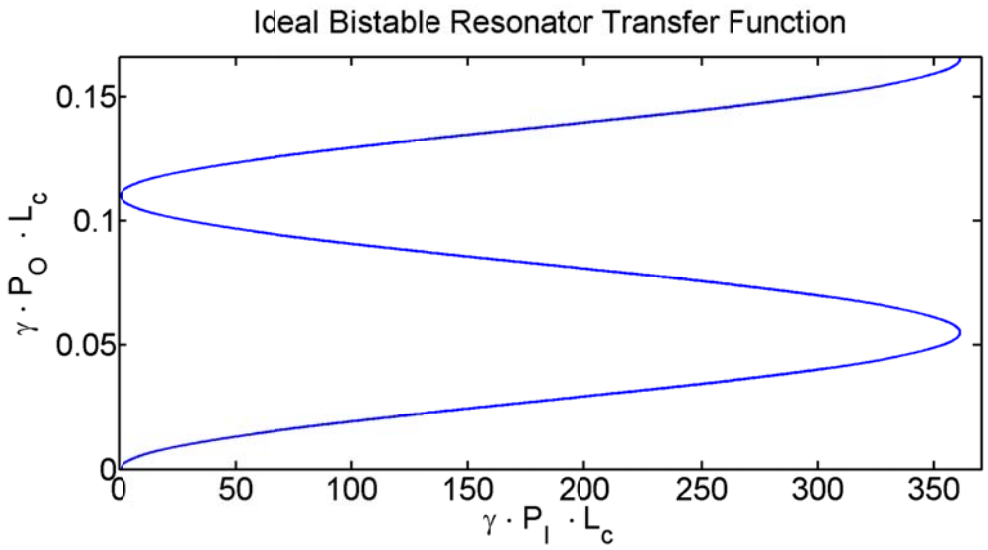

Fig. 5.1 Transfer function of a bistable lossless symmetric resonator in which $R = 0.9$, and $T = 0.1$ at a point of linear resonance.

5.4. Acknowledgements

This chapter, in part, is a reprint of "Optical Bistability in a Silicon Waveguide Distributed Bragg Reflector Fabry-Pérot Resonator" by A. Grieco, B. Slutsky, D.T.H. Tan, S. Zamek, M. P. Nezhad, and Y. Fainman as it appears in the Journal of Lightwave Tecnology, volume 30, Institute of Electrical and Electronics Engineers (IEEE), 2012. The dissertation author was the primary author of this paper.

6. Waveguide Fabrication

6.1. Fabrication Overview

The waveguides produced to demonstrate the proposed characterization methods were fabricated using a CMOS-compatible silicon-on-insulator material system [19], [11], [15]. A cross-sectional illustration of the fabrication process is provided in Fig. 6.1. Fabrication begins with a heterogeneous wafer composed of a 250 nm silicon layer on top of a 3 μm buried silicon dioxide layer on top of a thick silicon substrate (step 1 in Fig. 6.1). The top silicon layer is then coated with a layer of hydrogen silsesquioxane (HSQ) resist (step 2 in Fig. 6.1) that is patterned via electron beam lithography (step 3 in Fig. 6.1), and developed so that it forms a mask with the lateral dimensions of the desired waveguide (step 4 in Fig. 6.1). The wafer then undergoes an inductively coupled plasma reactive-ion etching process that removes the silicon not protected by the HSQ mask (step 5 in Fig. 6.1). The patterned silicon is then cladded with a layer silicon dioxide deposited via plasma-enhanced chemical vapor deposition, which completes the waveguide (step 6 in Fig. 6.1). The waveguides are then exposed by dicing or cleaving if necessary.

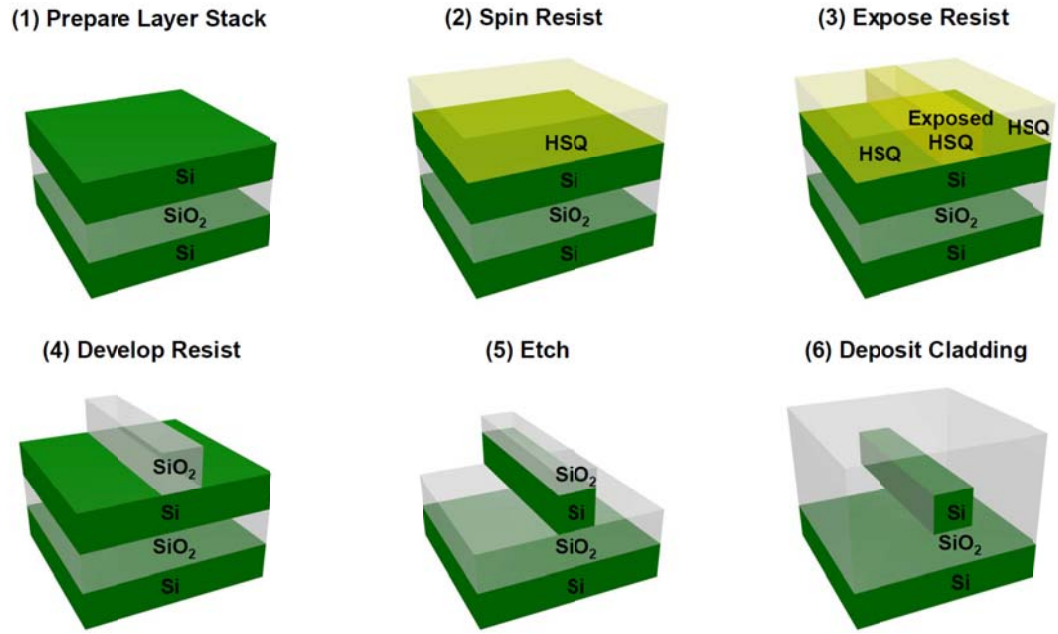

Fig. 6.1 Cross-sectional illustration of the fabrication process.

6.2. Thin Film Preparation

Waveguide fabrication begins with a layer stack of thin films. These films are films are prepared using commercial technology. In the case that a single crystalline film is required within the layer stack, the production of the film is outsourced. In the case of amorphous films the production is accomplished using plasma-enhanced chemical vapor deposition, using the recipes recommended by the manufacturer of the machine. The primary caveat with this technology is that the deposition rate can be dependent on chamber condition (the other film parameters such as refractive index remain consistent). This appears to be related to the history of films deposited since the last chamber clean, which can accumulate varying conditions such as intrinsic stress depending on the specific interfaces. Fortunately there are methods of compensating this variability. The first strategy is to precondition the chamber before

performing the desired deposition. This involves depositing a film of the desired material in the empty chamber to help create more uniform deposition conditions. The second strategy is to measure the actual deposition rate by halting the process approximately half way through. This may be accomplished with high confidence with a method such as reflectometry by including a small blank wafer in addition to the sample that requires deposition, and measuring the resulting two layer stack. The observed deposition rate is highly uniform over the course of a single deposition (even for a relatively thick film), so this method produces extremely accurate film thicknesses.

6.3. Lithography

The preparation of scientific nanophotonic devices is essentially a process of rapid prototyping. In this context, electron-beam lithography is generally more efficient than photolithography. This is because electron-beam lithography systems operate by scanning the beam, and each pattern is defined using a computer-aided design file. Photolithography systems require the generation of a separate physical photomask for each sample, which is a time consuming process. To produce the most consistent results, a dose test should be performed for each distinct combination of layerstack and resist, as the scattering characteristics will generally be different for each. Finally, in the context of photonics extra care should be taken in the selection of resist. This is because if the optical properties of the exposed and developed resist are appropriate, it can be used as waveguide cladding. This also reduces sample handling, as it is not necessary to remove the resist following exposure. For example, the

electron sensitive resist hydrogen silsesquioxane converts to silicon dioxide upon exposure and development, which is a common cladding employed in silicon waveguides [11], [19].

6.4. Etching

The physical definition of the waveguide is accomplished by selectively etching the portion of the thin film that is not protected by the lithography resist. Etching can be accomplished chemically, although this process can be complicated by the tendency of the etch rate to depend anisotropically on crystal structure. For this reason the preferred alternative is the commercial technology of inductively coupled plasma reactive-ion etching, using the recipes recommended by the manufacturer. This process is notable in that it produces extremely vertical waveguide sidewalls. The primary caveat with this technology is that the rate can be dependent on chamber condition. The best strategy to compensate for this is to design the sample such that the underlying layer is an extremely resistance etch stop. In this situation the etch process can simply be run slightly long to ensure that the overlying layer is entirely removed. The other alternative is to clean the chamber each time prior to before performing the desired etching process. It should be noted that the sidewall roughness introduced during the etching step is generally the primary source of scattering loss in waveguides. This is plainly visible in Fig. 6.2, which contains an electron micrograph of an etched silicon-on-insulator wafer.

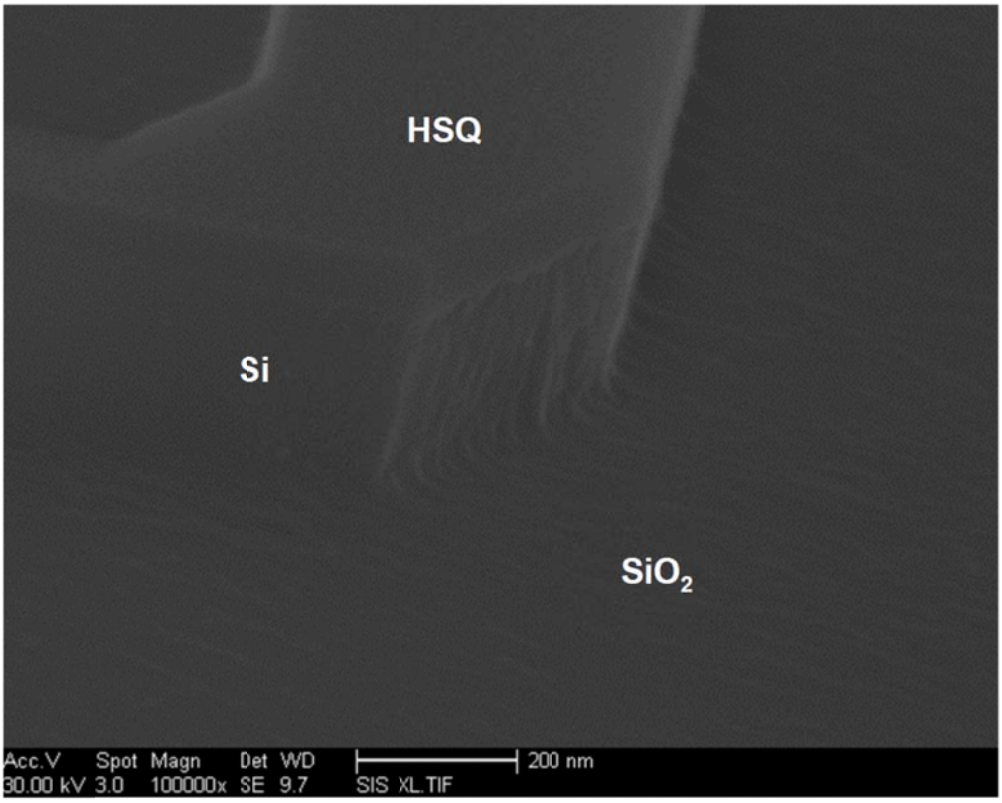

Fig. 6.2 Electron micrograph of an inductively coupled plasma reactive-ion etched silicon-on-insulator wafer taken at an angle of 80 degrees. The sidewall roughness of the HSQ mask is noticeably less than in the silicon.

6.5. Waveguide Access

Direct coupling methods require a way of accessing the waveguide cross section. This may be accomplished by cleaving or dicing the wafer. If the handle wafer on which the waveguide was prepared is crystalline, it is possible to cleave the wafer in a manner that will expose the waveguide. This method is not preferred, as there is a tendency for the cleave to drift over long distances (which is problematic for arrays of waveguides), and successful cleaving requires a delicate handle wafer (which precludes a physically robust device). Dicing essentially involves cutting the sample

with a very fine saw, and is therefore particularly suitable for samples which cannot be cleaved. The primary drawback of dicing is that the surface produced by the saw is rougher than the surface produced by cleaving, which will result in excess scattering loss at the interface. In the case of an amorphous cladding the best case roughness of the surface will be limited by the fracture pattern of the cladding material, for dicing or cleaving. If surface roughness is problematic, the quality of a surface can be improved by polishing. During polishing care must be taken to ensure the wafer is perpendicular to the grit and that parameters such as the wafer pressure are consistent, or the rate of material removal can vary wildly.

6.6. Acknowledgements

This chapter, in part, is a reprint of both "Optical Bistability in a Silicon Waveguide Distributed Bragg Reflector Fabry-Pérot Resonator" by A. Grieco, B. Slutsky, D.T.H. Tan, S. Zamek, M. P. Nezhad, and Y. Fainman as it appears in the Journal of Lightwave Tecnology, volume 30, Institute of Electrical and Electronics Engineers (IEEE), 2012, and "Characterization of waveguide loss using distributed Bragg reflectors" by A. Grieco, B. Slutsky, and Y. Fainman as it appears in Applied Physics B, volume 114, Springer, 2014, and "Characterization of Distributed Bragg Reflectors" by A. Grieco and Y. Fainman as it appears in the Journal of Quantum Electronics, volume 50, Institute of Electrical and Electronics Engineers (IEEE), 2014. The dissertation author was the primary author of these papers.

7. Experimental Design

7.1. Experimental Overview

Proper experimental demonstration of the methods described here requires care to eliminate potential sources of error. An illustrated schematic of the experimental setup employed in the demonstration of the characterization method is provided in Fig. 7.1 [19], [11], [15]. Device characterization is performed using a tunable laser to excite the desired mode of a given waveguide. The laser output is scrambled and repolarized to ensure the purity of the input polarization. Input coupling is accomplished by aligning a lensed fiber to the waveguide cross section. The transmitted light is collected by a microscope objective (lens 1 in Fig. 7.1). The collected light is imaged onto the detector by a pair of sequential 4F systems (comprised of lenses 1 and 2 and lenses 3 and 4 in Fig. 7.1). A spatial filter comprised of an iris in the initial focal plane is employed to isolate the output from a single waveguide and eliminate any stray light from the input fiber. A polarizer within a subsequent Fourier plane is used to reject any undesired polarization component that may result from imperfect alignment of the fiber, or which may arise from the device itself. A spectrometer may be used in place of the detector if it provides more suitable for the desired measurement. Likewise, a camera may be used temporarily in place of the detector for the purpose of inspecting the mode profile (in the far-field) or making coupling alignment more convenient. The measurements are automated by a computer which coordinates the tunable laser and power meter.

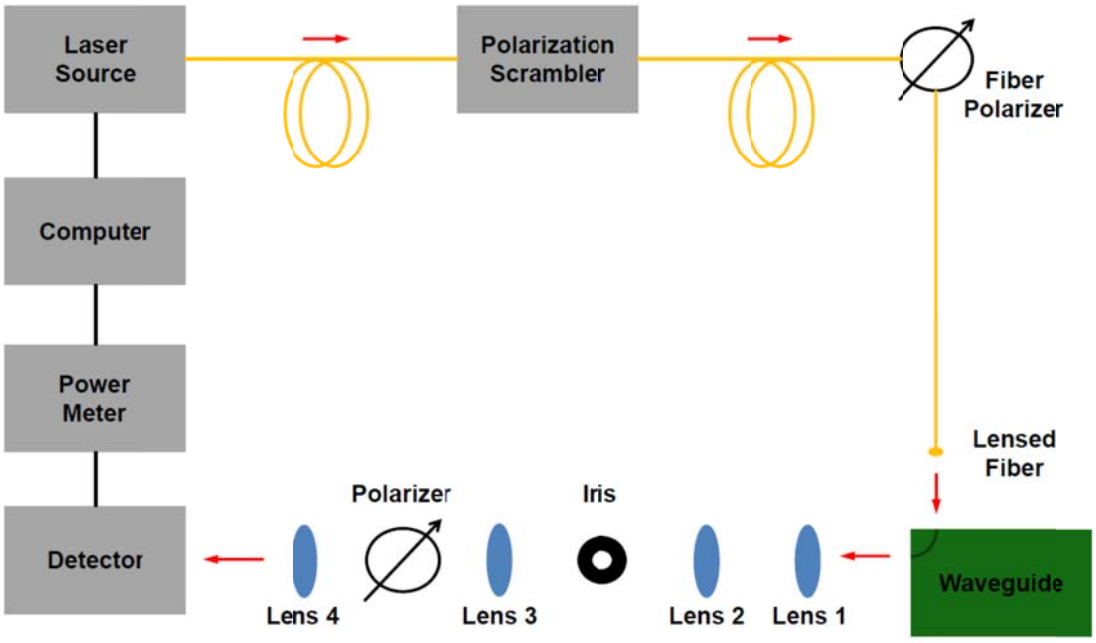

Fig. 7.1 Schematic experimental characterization setup.

7.2. Free-space versus Fiber

The preferred method of input coupling is through the direct overlap of the lensed fiber mode with the waveguide mode (either of which may be adiabatically tapered to improve mode matching [16]). This provides the maximum amount of wavelength independence, and allows the polarization to be controlled and verified using the camera by placing the input fiber at some point in the free-space optical path. The preferred method of output coupling is collection with a large aperture lens. This provides near perfect collection efficiency (which is much greater than could be accomplished using a lensed fiber output due to mode mismatch). Furthermore, a free-space output path provides more freedom than a fiber output. It allows spatial filtering to isolate the waveguide output, and visualization of the mode cross section using a camera. Fiber-to-fiber coupling systems are limited to guiding alignment by observing

waveguide scattering from a top-down camera. This becomes problematic for both extremely lossy waveguides (since the scattering intensity may not be visible at the output), and extremely low loss waveguides (since the scattering intensity will be negligible). Finally, a free-space system allows more freedom for accomplishing various optical operations, such as polarization control and wavelength filtering.

7.3. Waveguide Design

The methods of characterization described here involve specific interacting waveguide modes. In principle the interacting modes are specified by the phase matching condition. In the strictest sense, however, some small fraction of energy will be coupled into each guided mode by a perturbation. It is possible to minimize the experimental effect of this coupling by designing the waveguide geometry such that it only supports a single symmetric and antisymmetric mode of each polarization. The overlap integral of a symmetric and antisymmetric mode with a symmetric perturbation will be negligible. If it is necessary to use a waveguide with many modes, a device exists that allows the selective excitation of one mode from another [23]. The isolation of this device is very good, but the energy coupled from the light source into the modes that do not interact is lost.

7.4. Acknowledgements

This chapter, in part, is a reprint of both “Optical Bistability in a Silicon Waveguide Distributed Bragg Reflector Fabry-Pérot Resonator” by A. Grieco, B. Slutsky, D.T.H. Tan, S. Zamek, M. P. Nezhad, and Y. Fainman as it appears in the Journal of Lightwave Tecnology, volume 30, Institute of Electrical and Electronics

Engineers (IEEE), 2012, “Characterization of waveguide loss using distributed Bragg reflectors” by A. Grieco, B. Slutsky, and Y. Fainman as it appears in Applied Physics B, volume 114, Springer, 2014, and “Characterization of Distributed Bragg Reflectors” by A. Grieco and Y. Fainman as it appears in the Journal of Quantum Electronics, volume 50, Institute of Electrical and Electronics Engineers (IEEE), 2014. The dissertation author was the primary author of these papers.

Appendix

This appendix contains the derivation of the Fourier coefficients of the most common waveguide perturbations used in distributed Bragg reflectors. It is informative to begin by considering some general properties of Fourier series [24]. A periodic function $f(z)$ may be decomposed as the series:

$$f(z) = \sum_{k=-\infty}^{\infty} c_k \exp\left(-ik\frac{2\pi}{\Lambda}z\right), \tag{A.1}$$

$$c_k = \frac{1}{\Lambda}\int_0^{\Lambda} f(z)\exp\left(ik\frac{2\pi}{\Lambda}z\right)dz, \tag{A.2}$$

where k is an integer, and Λ is the period length. In accordance with Euler's law the coefficients may be rewritten as:

$$c_k = \frac{1}{\Lambda}\int_0^{\Lambda} f(z)\cos\left(k\frac{2\pi}{\Lambda}z\right)dz + i\frac{1}{\Lambda}\int_0^{\Lambda} f(z)\sin\left(k\frac{2\pi}{\Lambda}z\right)dz\,. \tag{A.3}$$

Such that if $f(z)$ is a real function the first term of Eq. (A.3) represents the real part of c_k and the second term represents the imaginary part of c_k. From the form of Eq. (A.3) it is also apparent that if the function is symmetric or antisymmetric about the point z = Λ/2, the coefficients undergo the following simplification:

$$c_k^{symmetric} = \frac{1}{\Lambda}\int_0^{\Lambda} f(z)\cos\left(k\frac{2\pi}{\Lambda}z\right)dz = \frac{2}{\Lambda}\int_0^{\frac{\Lambda}{2}} f(z)\cos\left(k\frac{2\pi}{\Lambda}z\right)dz,$$

(A.4)

$$c_k^{antisymmetric} = i\frac{1}{\Lambda}\int_0^{\Lambda} f(z)\sin\left(k\frac{2\pi}{\Lambda}z\right)dz = i\frac{2}{\Lambda}\int_0^{\frac{\Lambda}{2}} f(z)\sin\left(k\frac{2\pi}{\Lambda}z\right)dz,$$

(A.5)

where the superscripts indicate the relevant function type. It follows from Eqs. (A.4) and (A.5) that the Fourier coefficients of symmetric real functions are real, while the Fourier coefficients of antisymmetric real functions are imaginary. Another notable property of real functions $f(z)$ that follows from simple inspection of Eq. (A.2) or Eq. (A.3) is that the coefficients obey the relationship $c_k = c_{-k}^*$.

The first common perturbation is a square wave composed of alternating materials such that the permittivity may be described as:

$$\Delta\varepsilon(x,y,z) = \Delta\varepsilon(x,y)\begin{cases} 1, & 0 < z < \dfrac{\Lambda}{2} \\ -1, & \dfrac{\Lambda}{2} < z < \Lambda \end{cases},$$

(A.6)

$$\Delta\varepsilon(x,y) = \varepsilon_0(x,y)\begin{cases} \dfrac{n_1 - n_2}{2}, & \text{perturbed cross section} \\ 0, & \text{elsewhere} \end{cases},$$

(A.7)

where $\Delta\varepsilon$ is the perturbed permittivity, n_1 and n_2 are the indices of refraction of the alternating materials, and Λ is the perturbation period. For the purpose of calculating the unperturbed modes, the unperturbed permittivity ε of the perturbation region should be taken as:

$$\varepsilon(x,y)=\varepsilon_0(x,y)\frac{n_1+n_2}{2}. \tag{A.8}$$

Since the perturbation is antisymmetric, the Fourier coefficients may be calculated using Eq. (A.5):

$$\begin{aligned} c_k &= i\frac{2}{\Lambda}\Delta\varepsilon(x,y)\int_0^{\frac{\Lambda}{2}}\sin\left(k\frac{2\pi}{\Lambda}z\right)dz = i\frac{2}{\Lambda}\Delta\varepsilon(x,y)\left[\frac{-\cos\left(k\frac{2\pi}{\Lambda}z\right)}{k\frac{2\pi}{\Lambda}}\right]\Bigg|_0^{\frac{\Lambda}{2}}. \\ &= \frac{i}{\pi k}\Delta\varepsilon(x,y)\left[1-\cos(k\pi)\right] \end{aligned} \tag{A.9}$$

Therefore from Eq. (A.9) the k^{th} Fourier coefficient of the perturbation may be expressed as:

$$\varepsilon_k = \begin{cases} \dfrac{2i}{\pi k}\Delta\varepsilon(x,y)=\dfrac{i(n_1+n_2)}{\pi k}\varepsilon_0(x,y), & k=odd \\ 0, & k=even \end{cases}. \tag{A.10}$$

The final common perturbation is a sine wave composed of alternating materials such that the permittivity may be described as a sine wave:

$$\Delta\varepsilon(x,y,z)=\Delta\varepsilon(x,y)\sin\left(\frac{2\pi}{\Lambda}z\right),$$

(A.11)

$$\Delta\varepsilon(x,y)=\varepsilon_0(x,y)\begin{cases}\dfrac{n_1-n_2}{2}, & \text{perturbed cross section}\\ 0, & \text{elsewhere}\end{cases},$$

(A.12)

where $\Delta\varepsilon$ is the perturbed permittivity, n_1 and n_2 are the indices of refraction of the alternating materials, and Λ is the perturbation period. For the purpose of calculating the unperturbed modes, the unperturbed permittivity ε of the perturbation region should be taken as:

$$\varepsilon(x,y)=\varepsilon_0(x,y)\frac{n_1+n_2}{2}.$$

(A.13)

Since the perturbation is antisymmetric and takes such a simple form, the Fourier coefficients may be determined essentially by inspection in conjunction with Eq. (A.5):

$$c_k=i\frac{1}{\Lambda}\Delta\varepsilon(x,y)\int_0^{\Lambda}\sin\left(\frac{2\pi}{\Lambda}z\right)\sin\left(k\frac{2\pi}{\Lambda}z\right)dz=\begin{cases}i\Delta\varepsilon(x,y), & k=1\\ 0, & k\neq 1\end{cases}.$$

(A.14)

Therefore from Eq. (A.14) the k^{th} Fourier coefficient of the perturbation may be expressed as:

$$\varepsilon_k = \begin{cases} i\Delta\varepsilon(x,y) = i\dfrac{n_1 - n_2}{2}\varepsilon_0(x,y), & k = 1 \\ 0 \qquad\qquad\qquad\qquad\quad , & k \neq 1 \end{cases}. \tag{A.15}$$

References

[1] J. D. Jackson, Classical Electrodynamics, 3rd ed., Hoboken, NJ: John Wiley & Sons, 1999.

[2] P. Yeh, Optical Waves in Layered Media, Hoboken, NJ: John Wiley & Sons, 2005.

[3] A. Yariv and P. Yeh, Optical Waves in Crystals: Propagation and Control of Laser Radiation, Hoboken, NJ: John Wiley & Sons, 2003.

[4] C. A. Balanis, Advanced Engineering Electromagnetics, Hoboken, NJ: John Wiley & Sons, 1989.

[5] M. Heiblum and J. H. Harris, "Analysis of Curved Optical Waveguides by Conformal Transformation," *Journal of Quantum Electronics,* Vols. QE-11, pp. 75-83, 1975.

[6] D. M. Shyroki, "Exact Equivalent Straight Waveguide Model for Bent and Twisted Waveguides," *Transactions on Microwave Theory and Techniques,* vol. 56, pp. 414-419, 2008.

[7] B. A. Saleh and M. C. Teich, Fundamentals of Photonics, Hoboken, NJ: John Wiley & Sons, 1991.

[8] H. Kogelnik, "2. Theory of Dielectric Waveguides," in *Integrated Optics (Topics in Applied Physics)*, Berlin, DE, Springer-Verlag, 1975, pp. 13-81.

[9] D. L. Lee, Electromagnetic Principles of Integrated Optics, Hoboken, NJ: John Wiley & Sons, 1986.

[10] G. P. Agrawal, Nonlinear Fiber Optics, 4th ed., San Diego, CA: Academic Press, 2006.

[11] A. Grieco, B. Slutsky and Y. Fainman, "Characterization of waveguide loss using distributed Bragg reflectors," *Applied Physics B,* vol. 114, pp. 467-474, 2014.

[12] Y. Wang, A. Grieco and T. Nguyen, "Allpass filter design with waveguide loss compensation," *Optics Express,* vol. 21, pp. 32040-32052, 2013.

[13] N. D. Sankey, D. F. Prelewitz and T. G. Brown, "All-optical switching in a nonlinear periodic-waveguide structure," *Applied Physics Letters,* vol. 60, pp. 1427-1429, 1992.

[14] Y. Painchaud, M. Poulin, C. Latrasse and M.-J. Picard, "Bragg grating based Fabry-Perot filters for characterizing silicon-on-insulator waveguides," in *IEEE 9th International Conference on Group IV Photonics (GFP)*, pp. 180-182, San Diego, California, Aug. 2012.

[15] A. Grieco and Y. Fainman, "Characterization of Distributed Bragg Reflectors," *Journal of Quantum Electronics,* vol. accepted for publication, 2014.

[16] V. R. Almeida, R. R. Panepucci and M. Lipson, "Nanotaper for Compact Mode Conversion," *Optics Letters,* vol. 28, pp. 1302-1304, 2003.

[17] D. Taillaert, F. Van Laere, M. Ayre, W. Bogaerts, D. Van Thorhout, P. Bienstman and R. Baets, "Grating Couplers for Coupling between Optical Fibers and Nanophotonic Waveguides," *Japanese Journal of Applied Physics,* vol. 45, pp. 6071-6077, 2006.

[18] W. A. Pasmooij, P. A. Mandersloot and M. K. Smit, "Prism-Coupling of Light into Narrow Planar Optical Waveguides," *Journal of Lightwave Technology,* vol. 7, pp. 175-180, 1989.

[19] A. Grieco, B. Slutsky, D. T. H. Tan, S. Zamek, M. P. Nezhad and Y. Fainman, "Optical Bistability in a Silicon Waveguide Distributed Bragg Reflector Fabry-Pérot Resonator," *Journal of Lightwave Technology,* vol. 30, pp. 2352-2355, 2012.

[20] P. Dong, W. Qian, S. Liao, H. Liang, C.-C. Kung, N.-N. Feng, R. Shafiiha, J. F. Fong, D. Feng, A. V. Krishnamoorthy and M. Asghari, "Low loss shallow-ridge silicon waveguides," *Optics Express,* vol. 18, pp. 14474-14479, 2010.

[21] W. R. McKinnon, D.-X. Xu, C. Storey, E. Post, A. Densmore, A. Delâge, P. Waldron, J. H. Schmidt and S. Janz, "Extracting coupling and loss coefficients from a ring resonator," *Optics Express,* vol. 17, pp. 18971-18982, 2009.

[22] H. M. Gibbs, Optical Bistability: Controlling Light With Light, New York, NY: Academic Press, 1985.

[23] K. Ikeda, M. Nezhad and Y. Fainman, "Wavelength selective coupler with vertical gratings on silicon chip," *Applied Physics Letters,* vol. 92, pp. 201111-1 - 201111-3, 2008.

[24] D. K. Frederick and A. B. Carlson, Linear Systems in Communication and Control, Hoboken, NJ: John Wiley & Sons, 1971.